

Article

Synthesis of Cobalt(III) Complexes Derived from Pyridoxal: Structural Cleavage Evaluations and In Silico Calculations for Biological Targets

Liniquer André Fontana¹, Francisco Mainardi Martins², Josiéli Demetrio Siqueira² , Carlos Serpa³ , Otávio Augusto Chaves^{3,4,*}  and Davi Fernando Back^{2,*}

¹ Institute of Chemistry, University of Campinas, Rua Josué de Castro, Cidade Universitária Zeferino Vaz, Campinas 13083-970, SP, Brazil; lfontana@unicamp.br

² Inorganic Materials Laboratory, Department of Chemistry, Center for Natural and Exact Sciences (CCNE), Federal University of Santa Maria (UFSM), Santa Maria 97105-900, RS, Brazil; chicommartins@gmail.com (F.M.M.); josielidemetrioss@gmail.com (J.D.S.)

³ Department of Chemistry, Coimbra Chemistry Centre—Institute of Molecular Science (CQC-IMS), University of Coimbra, Rua Larga s/n, 3004-535 Coimbra, Portugal; serpaso@ci.uc.pt

⁴ Laboratory of Immunopharmacology, Centro de Pesquisa, Inovação e Vigilância em COVID-19 e Emergências Sanitárias (CPIV), Oswaldo Cruz Institute (IOC), Oswaldo Cruz Foundation (Fiocruz), Rio de Janeiro 21040-361, RJ, Brazil

* Correspondence: otavioaugustochaves@gmail.com (O.A.C.); daviback@gmail.com (D.F.B.)

Abstract: This study sought to investigate the synthesis of eight complexes constituted by a cobalt(III) (Co^{III}) metallic center coordinated to two units of iminic ligands LnC ($n = 1-4$, **L1C-L4C**), which are derivatives of pyridoxal hydrochloride and anilines with thioether function containing one to four carbons. Depending on the source of the cobalt ion and the addition (or not) of a non-coordinating counterion, complexes with distinct structures may form, being categorized into two series: $[\text{Co}^{\text{III}}(\text{LnC})(\text{L0C})]$ ($n = 1-4$, **C1'-C4'**) with a LnC ligand and a ligand that has a thiolate function which cleaves the C-S(thioether) bond (**L0C**) and $[\text{Co}^{\text{III}}(\text{LnC})_2]\text{PF}_6$ ($n = 1-4$, **C1-C4**) with two similar units of the same LnC ligand. The occurrence (or not) of cleavage in the eight complexes was observed by elucidating the solid-state structures by single crystal X-ray diffraction. This exciting method allows the synthesis of Co^{III} complexes without cleaving the C-S bonds from the ligands, thereby not requiring an inert atmosphere in the reaction systems. The synthesized complexes were evaluated by in silico calculations on viable biological targets such as deoxyribonucleic acid, superoxide dismutase enzyme, human serum albumin, and the structural spike glycoprotein of severe acute respiratory syndrome coronavirus 2 (SARS-CoV-2) with the receptor binding domain (RBD) in both up and down conformations without and in complex with the cellular receptor angiotensin-converting enzyme 2 (ACE2). Overall, in silico results suggested that all the inorganic complexes under study are potential anticancer/antiviral agents; however, **C4** and **C4'** are the best candidates for future in vitro assays.

Keywords: pyridoxal; cleavage; Co^{III} complexes; C-S(thioether); in silico calculations; anticancer; antiviral



Citation: Fontana, L.A.; Martins, F.M.; Siqueira, J.D.; Serpa, C.; Chaves, O.A.; Back, D.F. Synthesis of Cobalt(III) Complexes Derived from Pyridoxal: Structural Cleavage Evaluations and In Silico Calculations for Biological Targets. *Inorganics* **2024**, *12*, 171. <https://doi.org/10.3390/inorganics12060171>

Academic Editors: Snežana Jovanović-Stević and Jovana V. Bogojeski

Received: 17 April 2024

Revised: 11 June 2024

Accepted: 16 June 2024

Published: 18 June 2024



Copyright: © 2024 by the authors. Licensee MDPI, Basel, Switzerland. This article is an open access article distributed under the terms and conditions of the Creative Commons Attribution (CC BY) license (<https://creativecommons.org/licenses/by/4.0/>).

1. Introduction

Carbon–sulfur bonds of specific organosulfur compounds, such as C(alkyl)-S and C(aryl)-S [1], can be catalytically activated by thiophilic metal ions and undergo cleavage and subsequent transformation [2]. This process can be led by transition metal centers and their compounds forming new sulfur molecules or sulfide-containing complexes [1]. These metal ion-mediated cleavages and transformation processes of C-S bonds are important in the oil and fuel industries [3], synthetic chemistry [4], and biological mechanisms [4], including the functioning of the enzyme methyl-coenzyme M reductase [5].

Recent reports have described the cleavage of C-S bonds by the action of different transition metal ions, such as palladium [6,7], iron [8], rhodium [1,9], copper [10], nickel [4], and cobalt [11–15]—a trace element essential for human life [16]. The catalytic action of cobalt as a constituent of cobalamin (vitamin B12) stands out [17], as it is a crucial part of DNA synthesis and cellular energy production [18]. In mammals, its forms containing methyl and adenosyl ligands are present as a cofactor of two enzymes: methionine synthase and methylmalonyl-CoA mutase [17–19]. Cobalt(II) (Co^{II}) forms labile high-spin complexes with different possible coordination numbers. In contrast, cobalt(III) (Co^{III}) has octahedral coordination with high or low spin configurations, the latter being inert for ligand substitution and diamagnetic due to the d^6 configuration [20].

To improve processes involving C-S bond activation, the rational design and synthesis of ligands are fundamental since their characteristics (e.g., size and coordinating capacities of these molecules) influence the properties of metallic centers [9]. Among the possibilities, there are Schiff base ligands—organic compounds with C=N (imine) bonds [21]. Thus, to coordinate with octahedral metallic centers (e.g., Co^{III}), an interesting iminic ligand can be obtained by condensing derivatized anilines and aldehydes [22,23], most notably pyridoxal. This vitamin B6 derivative has structural diversity [24,25] and groups that form possible intermolecular interactions [26] including coordination with different charges and Pearson's absolute hardnesses, e.g., phenol/phenolate oxygen and imine nitrogen [27].

The design and development of drugs containing metal ions (metallo drugs) have gained significant attention in recent years for their potential applications in cancer and viral treatments [28,29]. One of the most well-known metallo drugs used in cancer therapy is cisplatin and its derivatives, carboplatin and oxaliplatin. These complexes have the capacity to bind to deoxyribonucleic acid (DNA), causing structural changes that inhibit cell division and promote apoptosis [30,31]. However, novel metallo drugs have been designed to also inhibit specific enzymes crucial for cancer cell survival and generate reactive oxygen species (ROS) to induce oxidative stress and apoptosis selectively, e.g., platinum- and palladium-based compounds [32–37]. Interestingly, some reports correlated the severe acute respiratory syndrome coronavirus 2 (SARS-CoV-2) infection with increasing probability of cancer development in different organs [38–40] and due to the unique mechanisms of action and the versatility of metallo drugs in interacting with biological molecules, e.g., targeting specific crucial steps for cancer cells and also interfering with the viral replication process, either by directly targeting viral components or by modulating host cellular mechanisms, metallo drugs might represent a promising frontier in both cancer and antiviral therapies [41,42]. In this sense, cobalt Schiff base complexes have gained attention, mainly due to their ability to induce apoptosis in cancer cells [43,44] and inhibit viral replication by targeting different viral enzymes [45,46], which offers a promising avenue for the development new therapies.

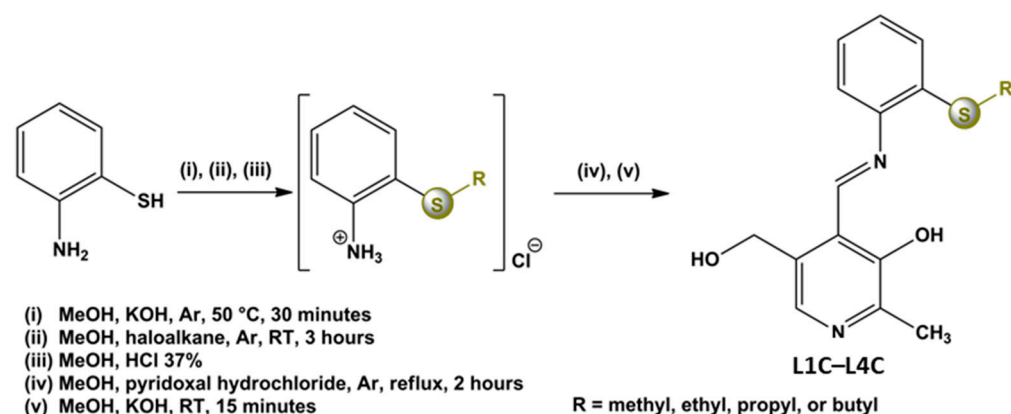
Thus, the present work reports the synthesis of a series of Schiff bases derived from pyridoxal and S-alkylated anilines containing different substituents, e.g., methyl, ethyl, propyl, and butyl, resulting in monomers containing Co^{III} cations. Depending on the conditions employed during the synthesis, bond cleavages between carbon and thioether atoms (C-sulfur) were observed. Additionally, molecular docking calculations were performed for $[\text{Co}^{\text{III}}(\text{LnC})_2]\text{PF}_6$ ($n = 1-4$, **C1-C4**) and $[\text{Co}^{\text{III}}(\text{LnC})(\text{L0C})]$ ($n = 1-4$, **C1'-C4'**) series complexes concerning their interactive profile with deoxyribonucleic acid (DNA), human serum albumin (HSA), and superoxide ions to preliminarily evaluate their anticancer profiles. Finally, the Co^{III} complexes were also *in silico* evaluated with the structural spike protein of severe acute respiratory syndrome coronavirus 2 (SARS-CoV-2) with receptor binding domain (RBD) in both up and down conformations without and in complex with the cellular receptor angiotensin-converting enzyme 2 (ACE2) due to the correlation between SARS-CoV-2 infection and oncogenesis [47]. The *in silico* results and their corresponding trends were compared with experimental data from the literature for other cobalt complexes. The novelty of this study lies in the relationship between the calculated *in silico*

activity and the differentiation of the complexes that showed C-S(thioether) bond cleavage and those that did not.

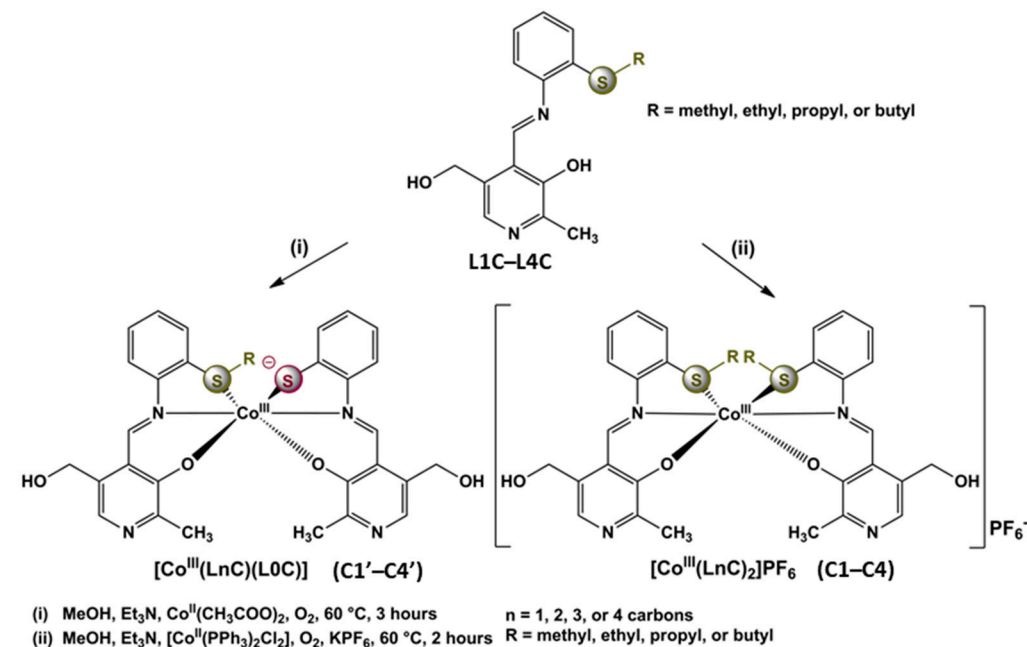
2. Results and Discussion

2.1. $[\text{Co}^{\text{III}}(\text{LnC})(\text{L0C})]$ Series Complexes (C1'–C4')

The iminic ligands (**L1C–L4C**) were synthesized in an inert argon atmosphere using dry methanol, as summarized in the synthetic pathways in Scheme 1. On the other hand, the complexation reactions between ligands **L1C–L4C** and Co^{II} acetate were done by bubbling atmospheric air every hour in the reactive medium, as summarized in the synthetic pathways in Scheme 2. In this case, a series of mononuclear complexes $[\text{Co}^{\text{III}}(\text{LnC})(\text{L0C})]$ ($n = 1–4$, C1'–C4') was obtained. The ORTEP-3.1 diagrams of the molecular structures of the $[\text{Co}^{\text{III}}(\text{LnC})(\text{L0C})]$ series complexes (C1'–C4') in the solid state are illustrated in Figure 1.



Scheme 1. General representation for the synthesis of S-alkylated anilines and **L1C–L4C** ligands.



Scheme 2. Synthesis of cobalt complexes of the series $[\text{Co}^{\text{III}}(\text{LnC})(\text{L0C})]$ ($n = 1–4$, C1'–C4') and $[\text{Co}^{\text{III}}(\text{LnC})_2]\text{PF}_6$ ($n = 1–4$, C1–C4) from **L1C–L4C** ligands according to the reagents used. For better interpretation the crystallization solvates were not shown.

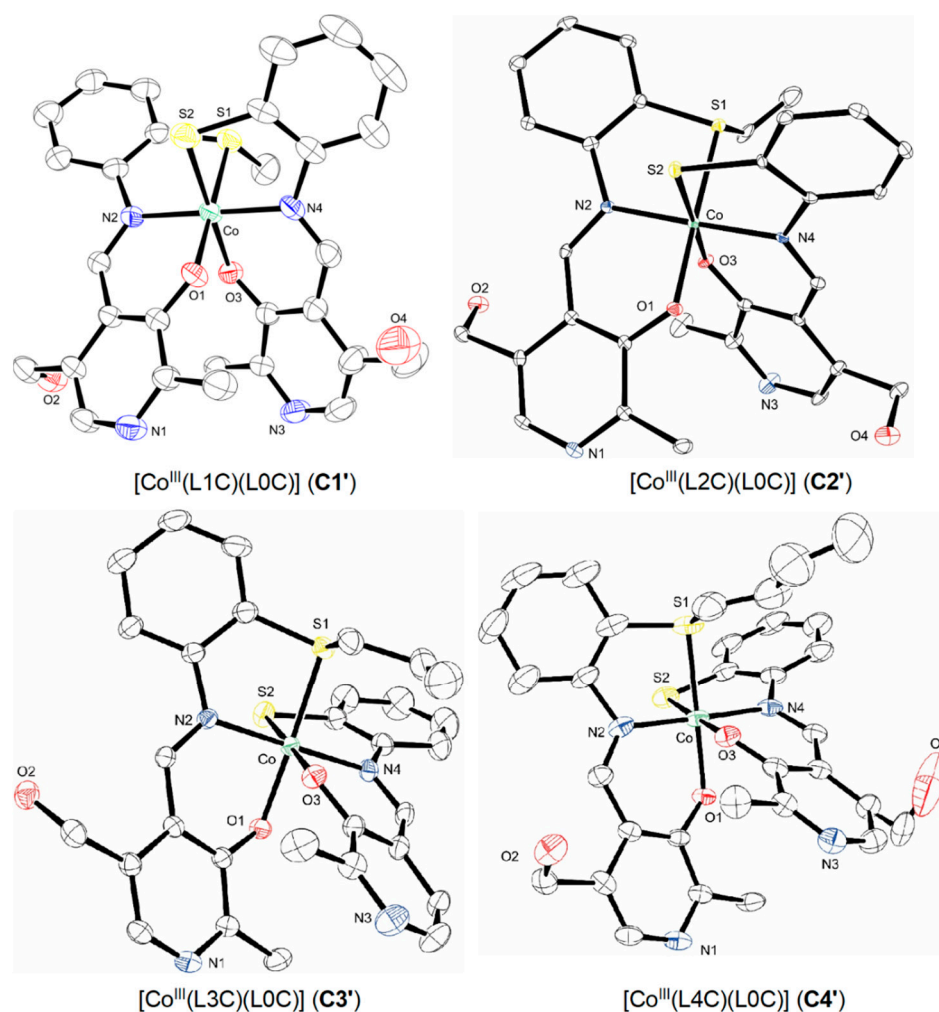


Figure 1. ORTEP-3.1 projection of the molecular structures of the [Co^{III}(LnC)(L0C)] series complexes (C1'–C4') in the solid state. Ellipsoids were calculated at 50% probability, and hydrogens and crystallization solvate are omitted for better visualization. In the case of the C1' complex, solvates from the starting material are not represented.

In this series of Co^{III} complexes, two distinct ligands coordinate with the cobalt cation were obtained. In the LnC form, coordination occurs by phenolate oxygen, imine nitrogen, and thioether sulfur atoms, being monoanionic species by the deprotonation of phenol. In the second form, L0C, the coordination occurs between a phenolate oxygen, imine nitrogen, and thiolate sulfur atom. The last highlighted organic function was formed in situ by the scission of the bond between carbon and thioether sulfur, which lost the aliphatic carbon chain. Thus, this thiolate anionic function with the charge of the phenolate oxygen makes L0C a dianionic ligand.

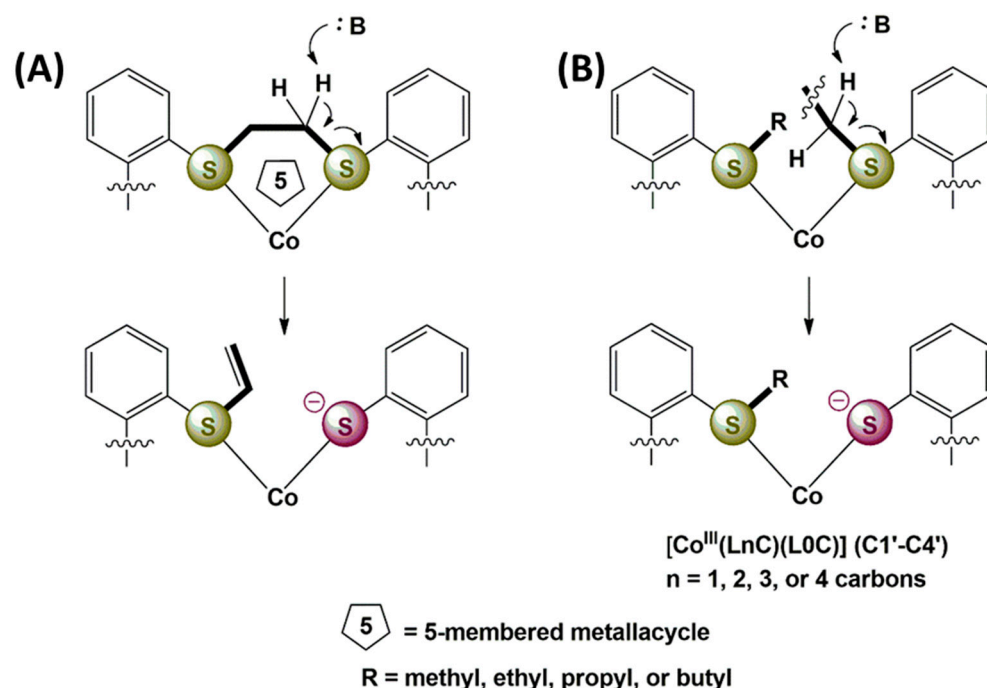
In the C1'–C4' compounds, the coordination of the ligands LnC in the monoanionic form and L0C in the dianionic form led to the formation of a neutral complex, and the cobalt metallic centers presented a trivalent oxidation state of the O₂N₂S₂ type. The bond length and angle values related to the coordination spheres of the C1'–C4' complexes and their respective comparisons with values in the literature are summarized in Table 1. It was noted that the bond length values converged with each other for Co^{III}-N(imine), Co^{III}-O(phenolate), Co^{III}-S(thioether), and Co^{III}-S(thiolate) bonds.

Table 1. The bonds' length and angle values related to the coordination spheres of the [Co^{III}(LnC)(LOC)] (C1'–C4') complex series and their respective comparisons with values found in the literature.

Parameter	Co ^{III} -Donor Atom	C1'	C2'	C3'	C4'	Literature
Bonds lengths (Å)	Co ^{III} -N(iminic)	1.911 (3)	1.915 (4)	1.924 (2)	1.897 (5)	1.913 (3) [14]
		1.919 (3)	1.918 (4)	1.936 (2)	1.904 (5)	1.926 (2) [14]
						1.903 (2) [48]
						1.910 (2) [48]
	Co ^{III} -O(phenolate)	1.900 (3)	1.916 (3)	1.9187 (19)	1.903 (3)	1.894 (2) [14]
		1.920 (3)	1.917 (3)	1.9311 (19)	1.927 (3)	1.914 (2) [14]
	Co ^{III} -S(thioether)	2.2193 (12)	2.2444 (14)	2.2485 (10)	2.2379 (15)	2.2274 (9) [14]
	Co ^{III} -S(thiolate)	2.2345 (13)	2.2330 (14)	2.2504 (10)	2.2377 (16)	2.2384 (9) [14] 2.237 (2) [48] 2.243 (1) [48]
Parameter	Donor Atom-Co ^{III} -Donor Atom	C1'	C2'	C3'	C4'	
Bonds angles (°)	O(phenolate)-Co ^{III} -N(imine)	86.83 (13)	86.77 (13)	88.26 (9)	88.33 (15)	
		87.89 (13)	87.44 (14)	89.53 (9)	88.35 (17)	
		92.60 (14)	94.05 (14)	92.40 (9)	92.00 (17)	
		93.09 (13)	94.10 (14)	93.24 (9)	93.37 (17)	
	O(phenolate)-Co ^{III} -O(phenolate)	89.07 (13)	87.65 (12)	86.45 (8)	88.22 (14)	
	N(imine)-Co ^{III} -N(imine)	178.86 (15)	178.31 (14)	177.19 (9)	178.27 (17)	
	O(phenolate)-Co ^{III} -S(thioether)	94.27 (9)	93.72 (10)	93.11 (7)	93.40 (11)	
		176.35 (10)	177.68 (10)	178.00 (6)	178.36 (11)	
	N(imine)-Co ^{III} -S(thioether)	88.57 (10)	87.83 (10)	85.64 (7)	86.45 (14)	
		90.48 (11)	91.26 (10)	93.72 (8)	91.83 (13)	
	O(phenolate)-Co ^{III} -S(thiolate)	92.13 (10)	94.64 (10)	93.11 (7)	93.12 (11)	
		178.76 (9)	176.92 (10)	179.42 (6)	178.49 (12)	
N(imine)-Co ^{III} -S(thiolate)	87.74 (12)	88.15 (10)	87.12 (8)	87.34 (14)		
	92.81 (11)	90.34 (10)	90.11 (7)	92.27 (14)		
S(thioether)-Co ^{III} -S(thiolate)	84.53 (5)	84.06 (6)	87.31 (4)	85.26 (6)		

The cleavage of C-S(thioether) bonds by cobalt ion was studied in hexadentate ligands derived from S-alkylated anilines containing two or three methylenes by different authors [11–15]. To obtain the C1'–C4' complexes, a similar method as previously reported was employed [13–15], in which Co^{II} acetate was used in the presence of dioxygen in the medium of the complexation reactions. An oxidative cleavage occurs in these cases, in which the carbon from methylene bonded to sulfur thioether is base-induced to activate, leading to its deprotonation and cleavage of the carbon–sulfur bond [15]. Recent evidence has suggested that oxygen is necessary in the reaction medium for the in situ oxidation of Co^{II} to Co^{III} and cleavage of the C-S bond [13,14].

In these studies, the authors reported that the cleavage requires the formation of a stable five-membered metallacycle between cobalt and thioether sulfurs (-S-Co-S-). Thus, the cleavage occurs to avoid forming an unfavorable four-membered ring [14,15]. In the present work, we extended the study of these cleavages to S-alkylated anilines with monohaloalkanes in initially tridentate ligands that, in turn, do not form such -S-Co-S- metallacycles (Scheme 3).



Scheme 3. (A) Carbon–sulfur bond cleavage in inorganic complexes from the literature in which there are five-membered -S-Co-S- metallacycles. (B) Carbon–sulfur bond cleavage in C1'–C4' complexes without the formation of the same -S-Co-S- metallacycles.

Interestingly, under favorable synthesis conditions, the cleavage of the bond between carbon and sulfur thioether occurs mainly by electronic factors. With the formation and coordination of an anionic sulfur thiolate, a better σ -donor, there is a better stabilization of the Co^{III} center, probably with a low spin. Furthermore, in the ligand-to-metal charge transfer (LMCT), sulfur in the form of thiolate is favored when cobalt is trivalent [13]. As the cleavage occurs in only one of the two ligands in the monoanionic form coordinated to the same metallic center, this phenomenon leads to the formation of a third anionic charge to stabilize the Co^{III} ion in the form of a neutral hexacoordinated complex.

Furthermore, Rajsekhar and coworkers [13,14] showed that cleavage of the C-S bond of hexadentate imine ligands derived from salicylaldehydes and S-alkylated aniline with two methylenes also occurs using other Co^{II} salts (i.e., hydrated chloride and sulfate). However, the authors found that the coordination reactions of the same ligands, although with Ni^{II} and Zn^{II} acetates, divalent metal ions with restricted redox behavior, do not lead the cleavage of the C-S bond and the formation of coordinated sulfur thiolate. In these two later cases, the formation of neutral complexes occurs by the coordination of the hexadentate ligand in the dianionic form to the Ni^{II} and Zn^{II} centers by sulfur thioether donor atoms [13,14].

2.2. $[Co^{III}(LnC)(L0C)]$ Series Complexes (C1–C4)

A mononuclear $[Co^{III}(LnC)_2]PF_6$ ($n = 1-4$, C1–C4) complex series was obtained after the reactions between the same ligands L1C–L4C (Scheme 1) but with the dichlorobis(triphenylphosphine)cobalt(II) ($Co^{II}Cl_2(PPh_3)_2$) complex as a source of cobalt cations and with the addition of potassium(I) hexafluorophosphate (KPF_6) in methanol in an open atmosphere (Scheme 2). The ORTEP-3.1 diagrams of the molecular structures of the $[Co^{III}(LnC)_2]PF_6$ series complexes (C1–C4) in the solid state are shown in Figure 2.

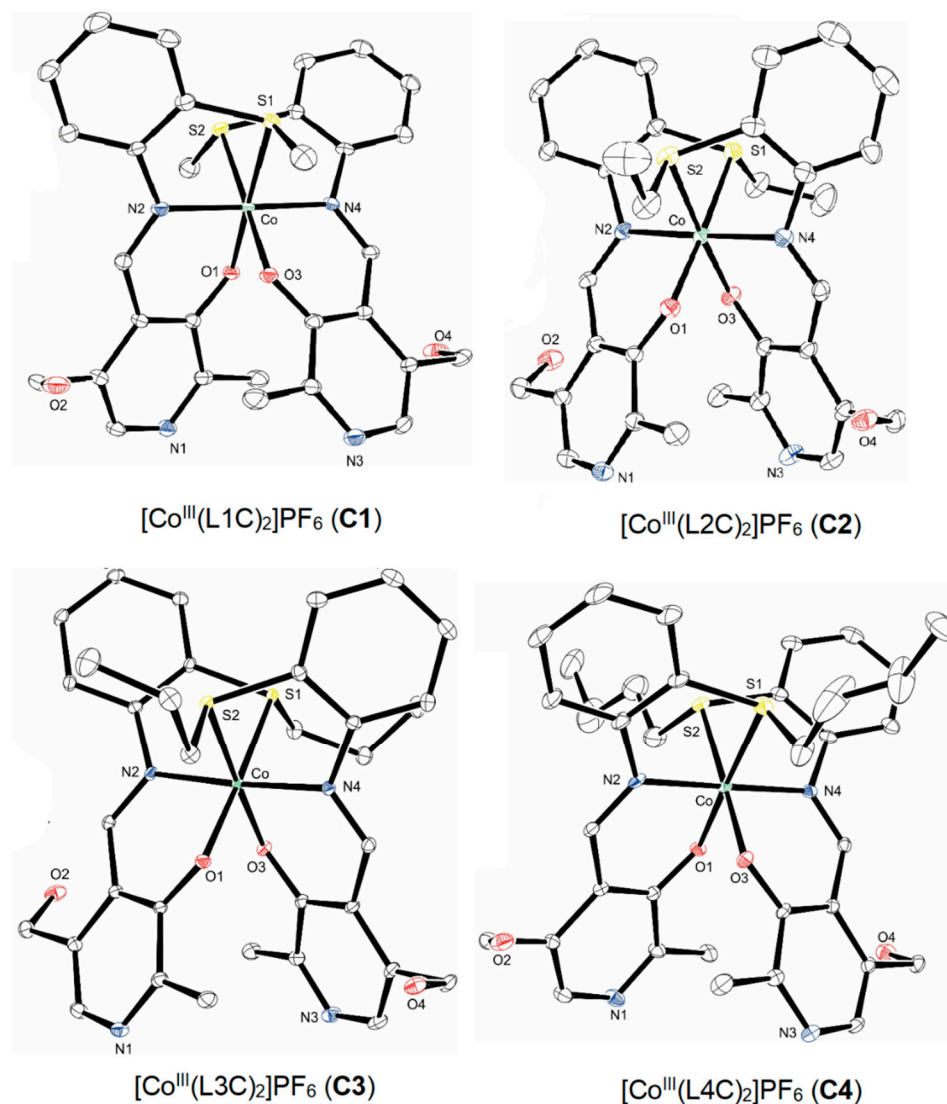


Figure 2. ORTEP-3.1 projection of the molecular structures of the $[\text{Co}^{\text{III}}(\text{LnC})_2]\text{PF}_6$ series complexes (**C1–C4**) in the solid state. Ellipsoids were calculated at 50% probability and hydrogens, crystallization solvates, hexafluorophosphate counterions (PF_6^-), and aniline molecules are omitted for better visualization.

In these four synthesized compounds, it was observed that two similar LnC ligands coordinated to the same metallic center via a phenolate oxygen atom, an imine nitrogen atom, and a thioether sulfur atom. Since thioether sulfur and imine nitrogen are neutral donor atoms and phenolic oxygen is deprotonated with (1-) charge, such LnC ligands are considered monoanionic.

Once the **C1–C4** complexes are isolated in the form of KPF_6 salt, a non-coordinating counterion with intense use in coordination chemistry, all complexes in this series can be denominated as monocationic complex ions. Thus, by the sum of the charges and coordination profile, it can be concluded that **C1–C4** also present trivalent cobalt species and the $\text{O}_2\text{N}_2\text{S}_2$ type.

Hence, in these cases, it is plausible that the air-stable phosphine–cobalt(II) complex [49] oxidizes from 2+ to 3+ in the reaction medium previously oxidized in the coordination to ligands **L1C–L4C**, preventing the cleavage of the carbon–sulfur bond and, consequently, without the formation of another anionic charge of the sulfur thiolate. The bond length and angle values related to the coordination spheres of the **C1–C4** complexes and their respective comparisons with values in the literature are summarized in Table 2.

It was noted that the bond length values converge with each other for Co^{III}-N(imine), Co^{III}-O(phenolate), Co^{III}-S(thioether), and Co^{III}-S(thiolate) bonds.

Table 2. The bonds' length and angle values related to the coordination spheres of the [Co^{III}(LnC)₂]PF₆ (C1–C4) complex series and their respective comparisons with values found in the literature.

Parameter	Co ^{III} -Donor Atom	C1	C2	C3	C4	Literature
Bond lengths (Å)	Co ^{III} -N(iminic)	1.925 (3)	1.916 (3)	1.9164 (13)	1.913 (3)	1.9224 (18) [50]
		1.927 (3)	1.923 (3)	1.9187 (13)	1.913 (4)	1.9248 (18) [50]
	Co ^{III} -O(phenolate)	1.878 (3)	1.883 (3)	1.8793 (11)	1.873 (3)	1.8809 (15) [50]
		1.880 (3)	1.883 (3)	1.8893 (10)	1.876 (3)	1.8870 (15) [50]
	Co ^{III} -S(thioether)	2.2423 (14)	2.2780 (15)	2.2684 (4)	2.2253 (13)	2.2494 (7) [50]
		2.2472 (14)	2.2840 (14)	2.2698 (4)	2.2456 (12)	2.2630 (6) [50]
Parameter	Donor Atom-Co ^{III} -Donor Atom	C1	C2	C3	C4	
Bonds angles (°)	O(phenolate)-Co ^{III} -N(imine)	86.23 (13)	89.61 (12)	90.49 (5)	86.10 (13)	
		86.97 (13)	89.82 (12)	90.79 (5)	86.85 (14)	
		93.89 (13)	91.35 (13)	91.95 (5)	93.83 (13)	
		94.40 (13)	91.81 (12)	92.41 (5)	94.20 (14)	
	O(phenolate)-Co ^{III} -O(phenolate)	88.92 (13)	89.28 (12)	87.83 (5)	89.03 (13)	
		N(imine)-Co ^{III} -N(imine)	178.62 (14)	178.12 (13)	176.08 (5)	179.26 (15)
	O(phenolate)-Co ^{III} -S(thioether)	92.03 (10)	90.94 (9)	91.32 (3)	91.44 (10)	
		92.59 (10)	91.99 (9)	92.92 (4)	92.82 (10)	
		177.41 (9)	176.82 (9)	177.15 (4)	177.35 (9)	
		178.40 (9)	177.45 (9)	177.65 (4)	178.12 (10)	
	N(imine)-Co ^{III} -S(thioether)	87.45 (11)	85.48 (11)	84.88 (4)	87.64 (11)	
		87.79 (11)	85.98 (9)	85.83 (4)	88.19 (11)	
		90.83 (11)	92.36 (10)	91.39 (4)	91.12 (12)	
		92.42 (10)	93.55 (10)	92.26 (4)	92.06 (10)	
S(thioether)-Co ^{III} -S(thiolate)	86.50 (6)	87.92 (4)	88.026 (15)	86.77 (5)		

2.3. In Silico Calculations on Feasible Biological Targets for Co^{III} Complexes

In silico calculations by molecular docking approach have become one of the most used tools in hit finding and hit-to-lead optimization at evaluating the drug targets via an atomic point of view of the binding capacity [51,52]. In this sense, molecular docking calculations for C1–C4 and C1'–C4' were performed with deoxyribonucleic acid (DNA), human serum albumin (HSA), and superoxide ions (O₂⁻) to suggest feasible biological targets (as anticancer agents), comparing the obtained in silico trend with experimental data previously reported in the literature for other cobalt complexes.

Genetic changes can lead to cancer if they alter the way that cells grow and spread. Some compounds, e.g., platinum complexes, can bind covalently between two strands of DNA (interstrand crosslinking agents) and thereby prevent vital processes such as replication or transcription in dividing cancer cells, and for this reason these are the first-line chemotherapy treatment for many solid human cancers [53,54]. Since platinum resistance in the treatment of malignant diseases has already been reported [55], there is still a necessity to identify novel inorganic complexes that might interact with DNA.

Table 3 summarizes the docking score values for the interactions of DNA: C1–C4/C1'–C4'. The highest docking score values were obtained in the minor groove of DNA, suggesting that the Co^{III} complexes might interact with DNA strands via the minor groove. Interestingly, the increase of carbon in the S-alkyl moieties of Co^{III} complexes improved their interactive profile with DNA. The main intermolecular forces responsible for this interaction are the van der Waals force and hydrogen bonding. The number of connecting points is higher for C1'–C4' than for C1–C4 with the corresponding lowest intermolecular distance (Table 4 and Figure 3). Thus, it is probable that C1'–C3' interact more strongly than

C1–C3 with DNA; however, the opposite trend was evidenced for **C4** and **C4'**, probably due to the lack of additional stabilization in **C4'** caused by the presence of just one S-alkyl group. Based on the reported literature [56], the Co^{III} complexes under study showed docking score values comparable with the experimental capacity of other cobalt complexes in interactions with DNA. In addition, the compounds **C4** and **C4'** showed better interactive profiles with DNA than the two reported water-soluble Co^{II} double-stranded helicates, $[\text{Co}^{\text{II}}_2\text{L}^2_2][\text{Co}^{\text{II}}(\text{NCS})_4]\bullet 9\text{H}_2\text{O}$ and $[\text{Co}^{\text{II}}_2\text{L}^4_2]\text{Cl}_2\bullet 11\text{H}_2\text{O}$, where L^2 and L^4 are also derived from pyridoxal [56].

Table 3. Molecular docking score values (dimensionless) for the interactions between the inorganic complexes **C1–C4/C1'–C4'** and DNA/HSA/spike and distances between $\text{O}_2^{\cdot-}$ and **C1–C4/C1'–C4'**.

Sample	DNA		HSA			SOD Mimetic	Spike Glycoprotein		Complex ACE2
	Major Groove	Minor Groove	Site I	Site II	Site III	Distance Complex: $\text{O}_2^{\cdot-}$ (Å)	Down Conformation	Up Conformation	
C1	36.8	38.3	20.1	----	24.6	1.70	47.8	37.3	36.0
C2	37.6	41.5	----	----	24.9	1.80	43.6	41.8	37.5
C3	40.6	44.5	10.3	----	17.2	2.00	46.6	42.8	42.1
C4	41.1	47.1	----	----	29.8	1.80	54.1	51.1	44.6
C1'	36.3	43.1	42.5	----	59.4	2.10	46.8	44.0	40.5
C2'	36.2	44.4	25.3	----	53.5	2.50	45.4	42.7	38.5
C3'	40.4	45.2	28.9	----	51.0	2.10	49.4	46.4	39.9
C4'	41.5	45.7	23.4	----	54.6	2.00	53.4	49.5	45.9

Table 4. Molecular docking results for the interactions between the inorganic complexes **C1–C4/C1'–C4'** and DNA/HSA.

Sample	Connected Points	Interactions	Distance (Å)
DNA: C1–C4	DG-04	Hydrogen bonding	2.80
	DC-21	Hydrogen bonding	3.10
	DG-22	Van der Waals	3.30
DNA: C1'–C4'	DC-03	Van der Waals	3.60
	DG-04	Hydrogen bonding	2.00
	DA-05	Van der Waals	2.50
	DG-22	Van der Waals	1.70
HSA: C1–C4	Arg-117	Hydrogen bonding	1.70
	Pro-118	Van der Waals	2.60
	Tyr-138	Van der Waals	1.30
	Pro-146	Van der Waals	3.00
	Phe-165	Van der Waals	2.10
	Leu-182	Van der Waals	3.00
	Arg-186	Van der Waals	3.70
HSA: C1'–C4'	Pro-118	Van der Waals	2.40
	Tyr-138	Van der Waals	3.60
	Ile-142	Van der Waals	1.00
	Tyr-161	Hydrogen bonding	2.00
	Phe-165	Van der Waals	2.80
	Leu-182	Van der Waals	2.70
	Arg-186	Hydrogen bonding	2.20
	Lys-190	Van der Waals	2.40

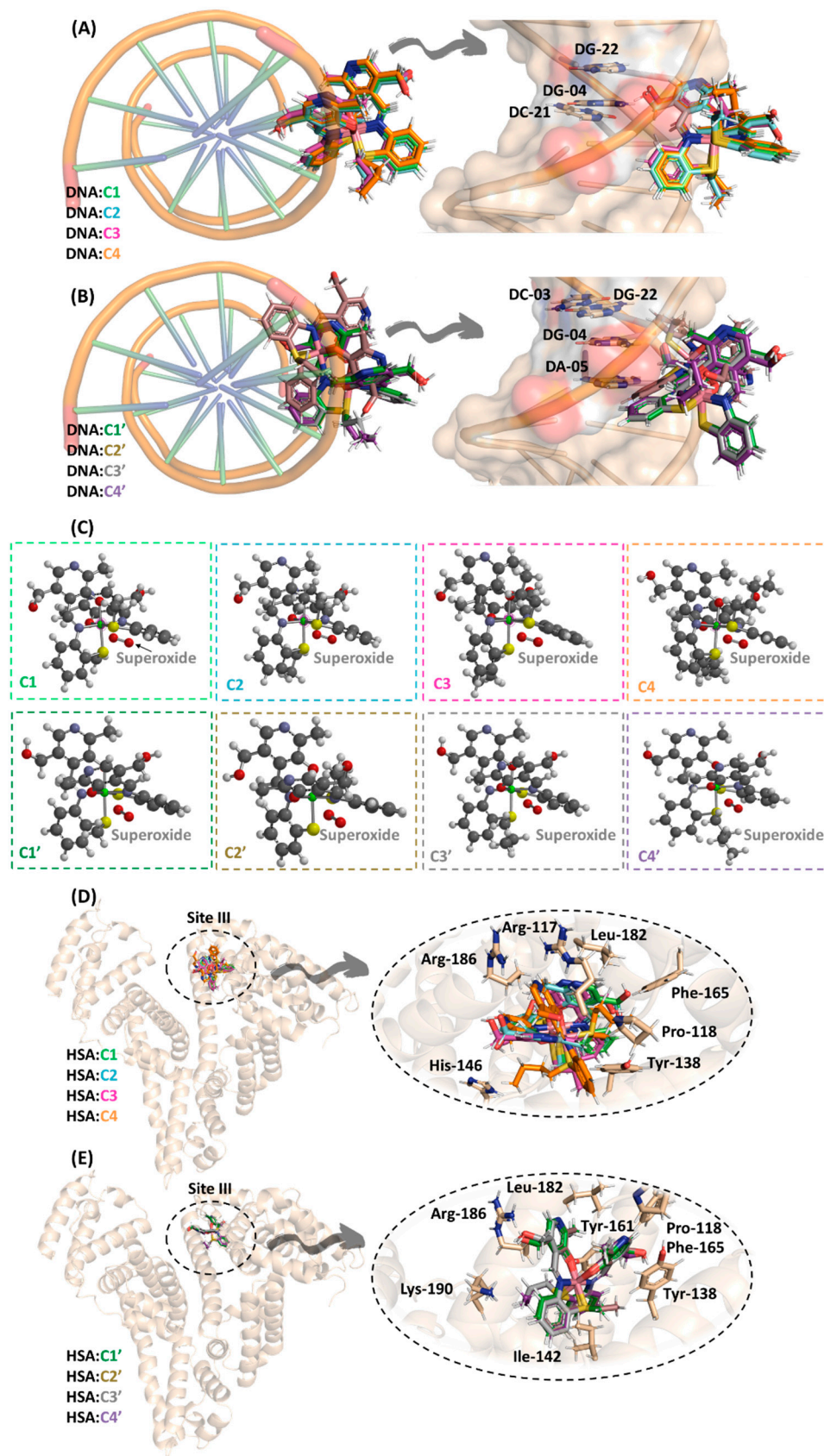


Figure 3. Top views and the corresponding identifications of the main nitrogenated bases that interact with (A) DNA: C1–C4 and (B) DNA: C1’–C4’ in the minor groove. (C) The representative distance

between the superoxide ion and each Co^{III} complex. Best docking pose and the corresponding zoom representation for the interactions of (D) HSA: C1–C4 and (E) HSA: C1'–C4' with subdomain IB (site III). Elements' color: hydrogen, nitrogen, oxygen, sulfur, and Co^{III} are in white, dark blue, red, yellow, and beige, respectively. In the case of SOD mimetics, the ion Co^{III} is represented in green.

Reactive oxygen species (ROS) are critical determinants of cellular signaling and a strict balance of ROS levels must be maintained to ensure proper cellular function and survival. Notably, ROS are increased in cancer cells, and the essential physiological role that the enzyme superoxide dismutase (SOD) plays in mitigating deleterious effects of ROS during oxidative stress caused by cancer cells has been reported on for this reason [57]. SOD has this capacity due to its redox-active metal ions in the active site (Fe-, Mn- or Cu, and Zn-SODs) which can react with superoxide ions (O_2^-) [58].

Thus, since the Co^{III} complexes showed good *in silico* interactive profiles with DNA, molecular docking calculations were also explored to suggest the capacity of these complexes to also interact with O_2^- and probably act as SOD mimetics. Table 3 summarizes the distance between O_2^- and the inorganic core of C1–C4/C1'–C4', showing a distance in the 1.70–2.50 Å range that is inside the previously reported theoretical distance correlated with *in silico* and biological data for SOD-mimetic compounds [27,59]. Overall, beyond the good interactive profile of DNA: C1–C4/C1'–C4', an inorganic core based on Co^{III} might interact with superoxide ions, also acting as a SOD mimetic. In this case, no trend based on the structural differences in the ligand structure was identified.

The most abundant globular protein in the human bloodstream is HSA (35–50 g/L), which is responsible for the delivery of both endogenous and exogenous compounds, e.g., fatty acids, hormones, metabolites, and commercial drugs, to their target [60,61]. Thus, since C1–C4 and C1'–C4' are potential DNA binders and SOD mimetics, it is interesting to evaluate, even only by *in silico* calculations, the capacity of these Co^{III} complexes to interact with HSA to offer preliminary insights into their pharmacokinetic profiles.

The HSA structure has three main binding sites: subdomain IIA (site I), located in a hydrophobic binding pocket, where the main fluorophore Trp-214 residue can be found; subdomain IIIA (site II), also located in a hydrophobic binding pocket; and subdomain IB (site III), located on the surface of the albumin [62]. As summarized in Table 3, site II was not identified as a feasible binding pocket for Co^{III} complexes; however, despite the compounds possibly interacting with sites I and III, the highest docking score values were obtained in subdomain IB, suggesting site III as the main binding pocket for the evaluated compounds. Differently to DNA binding, a trend based on the number of carbon atoms in the S-alkyl moieties was not identified for HSA; however, it was suggested that C1'–C4' have better interactive profiles than C1–C4 with HSA. Hydrogen bonding and van der Waals interactions are the main binding forces responsible for the stability of the interactions of HSA: C1–C4/C1'–C4' (Table 4 and Figure 3).

Comparing the obtained docking score values with those previously reported of other inorganic complexes that also bind into subdomain IB [63–65], it is probable that Co^{III} complexes might present low metabolization and high residence time in the human bloodstream (moderate binding affinity). Additionally, the evaluated compounds showed better interactive profiles with HSA than the *in silico* data reported on the Co^{II} double-stranded helicates $[\text{Co}^{\text{II}}_2\text{L}^2_2][\text{Co}^{\text{II}}(\text{NCS})_4]\cdot 9\text{H}_2\text{O}$ and $[\text{Co}^{\text{II}}_2\text{L}^4_2]\text{Cl}_2\cdot 11\text{H}_2\text{O}$, where L^2 and L^4 are also derived from pyridoxal [56], reinforcing C1–C4 and C1'–C4' as interesting compounds for future *in vitro* assays as anticancer agents.

During the pandemic scenario of coronavirus disease 2019 (COVID-19), different reports showed diverse life-threatening effects due to severe acute respiratory syndrome coronavirus 2 (SARS-CoV-2) infection. Like many oncogenic viruses, it has been hypothesized that SARS-CoV-2 employs various strategies to cause cancer in different organs [38–40]. Thus, since **C1–C4** and **C1'–C4'** showed *in silico* capacity to act as anticancer agents and SARS-CoV-2 infection might increase the probability of causing cancer, molecular docking calculations were also carried out on the spike glycoprotein of SARS-CoV-2 (wild type) with the receptor binding domain (RBD) in both up and down conformations without and in complex with the cellular receptor ACE2 to explore all feasible possibilities of interactions. This target was chosen due to the reports of other Co^{III} complexes in interactions with the spike glycoprotein of SARS-CoV-2 [66–68] and this multi-approach is important to identify the possibility of Co^{III} complexes to act as anticancer/antiviral metallodrugs.

The spike glycoprotein of SARS-CoV-2 contains RBD, which is a critical target for antiviral compounds due to its capacity in recognizing the cellular receptor ACE2. Fundamentally, RBD includes two structural domains: the core (highly conserved) and the external subdomains arranged into three homologous chains (A, B, and C, Figure 4). There is conformational equilibrium between the down and up conformations of RBD in the spike glycoprotein, i.e., the active conformation to interact with ACE2 is the up form [69]. Since there are not any experimental data available for Co^{III} complexes that identify the main mechanisms of interaction between these inorganic complexes and the spike glycoprotein, this work evaluated all the possibilities *in silico*. As summarized in Table 3, there is an increase in the molecular docking score values from the spike glycoprotein complexed with ACE2 to the spike glycoprotein with the three RBD in down conformations, e.g., 36.0, 37.3, and 47.8 dimensionless to **C1**, suggesting that all Co^{III} complexes might interact preferentially via a competitive mechanism. Interestingly, as depicted in Figure 4, **C1–C4** or **C1'–C4'** interact with the three RBD chains that are in the down conformation; however, when chain B is in the up conformation, the Co^{III} complexes are dislocated, indicating that chain B might be the main structural motif that interacts with the inorganic complexes under study. Additionally, the electrostatic potential map of the spike glycoprotein (Figure 4) suggests that this might occur due to the capacity of Co^{III} complexes to interact with positive binding pockets. Overall, all the inorganic complexes under study are potential anticancer/antiviral agents; however, **C4** and **C4'** are the best candidates for *in vitro* evaluations.

3. Materials and Methods

3.1. Materials and General Instrumentation

All reagents were of commercial grade and used as received. The synthetic procedures of the S-alkylated anilines and imine ligands have already been reported elsewhere (except for the L1C ligand, described herein) and were performed in dry methanol in an inert argon atmosphere system [23]. The complexation reactions were carried out with methanol without purification in an open atmosphere system.

Infrared spectra (FT-IR) were recorded using a Bruker Tensor 27 spectrometer (Bruker Corporation, Billerica, MA, USA) with dry KBr pellets in the 4000–400 cm^{-1} range with band intensities expressed as w (weak), m (medium), s (strong), and br (broad). UV-Vis absorption spectra were recorded on a Shimadzu UV-2600 spectrometer (Shimadzu Scientific Instruments, Inc., Columbia, MD, USA) using a quartz cuvette (1.0 cm) in *N,N*-dimethylformamide (DMF) solutions. The ^1H - and ^{13}C -nuclear magnetic resonance spectra (^1H - and ^{13}C -NMR) were recorded on a Bruker DPX-400 spectrometer (Bruker Corporation, Billerica, MA, USA). Deuterated dimethyl sulfoxide (DMSO-d_6) and deuterated chloroform (CDCl_3) were used as solvents, and tetramethylsilane (TMS) was used as the internal reference. The chemical shifts were expressed in δ (ppm), and the coupling constants (*J*) in Hz. Multiplicities were expressed as s (singlet), t (triplet), q (quartet, quintet, or sextet), m (multiplet), and br (broad).

3.2. X-ray Crystallography

Data were collected on a Bruker D8 Venture diffractometer (Bruker Corporation, Billerica, MA, USA) equipped with an Incoatec μS high brilliance Mo- $\text{K}\alpha$ X-ray tube with two-dimensional Montel micro-focusing optics and a Photon 100 detector. Measurements (C2', C3', C1, C3, and C4) were made at low temperature (100 K–120K) using a Cryostream 800 unit from Oxford Cryosystems (Hanborough Business Park, Long Hanborough, UK). The structures were solved by direct methods using SHELXS [70]. Fourier-difference map analyses yielded the positions of the non-hydrogen atoms. Refinements were carried out with the SHELXL package version 2018/3 [71]. All refinements were made by full-matrix least squares on F^2 with anisotropic displacement parameters for all non-hydrogen atoms. Hydrogen atoms were included in the refinement in calculated positions according to the molecular skeletons. Drawings were done using the software ORTEP-3.1 for Windows [72]. Crystal data and more details of the data collection and refinements of complexes C1'–C4' and C1–C4 are contained in Tables S1 and S2 in the Supplementary Materials, respectively.

3.3. S-Alkylated Aniline Synthesis

S-alkylated anilines were synthesized using dry methanol in an inert argon atmosphere. 2-Aminothiophenol (2.0 mmol, 0.250 g) was dissolved in 15 mL of methanol in a 50 mL round bottom flask, followed by the addition of potassium hydroxide (KOH, 2.0 mmol, 0.112 g). The resulting mixture was heated at 50 °C and kept under constant magnetic stirring for 30 min. Afterward, a methanolic solution (10 mL) containing the respective haloalkane (2.0 mmol) (iodomethane, ethyl bromide, propyl bromide, or butyl bromide) was added dropwise and the resulting reaction mixture was stirred at room temperature for 3 h. Methanol was then evaporated and the reaction was extracted with dichloromethane, which was evaporated. The resulting oil was dissolved in 10 mL of methanol and treated with concentrated hydrochloric acid (Scheme 1). The solvent was evaporated and the resulting solid was washed several times with diethyl ether and recrystallized from methanol. The compounds 2-(ethylthio)benzenamine hydrochloride, 2-(propylthio)benzenamine hydrochloride, and 2-(butylthio)benzenamine hydrochloride have been already published in our previous work [23]. The NMR, FT-IR, and UV-Vis spectra of S-alkylated anilines are presented in the Supplementary Material.

2-(Methylthio)benzenamine hydrochloride. Yield: 57%. Anal. Calcd for $\text{C}_7\text{H}_{10}\text{NSCl}(\%)$: C 47.86; H 5.74; N 7.97. Found (%): C 47.79; H 5.72; N 7.91. M.p. 160–162 °C. FT-IR (KBr pellets, cm^{-1}): 756 [m, $\nu(\text{C-S})$], 2865 [s, $\nu(\text{C-NH}_3^+)$], 1512 [m, $\nu(\text{C-NH}_3^+)$], 1566 [m, $\nu(\text{C=C}_{\text{ar}})$].

^1H NMR (400 MHz, DMSO- d_6 , δ in ppm): 2.47 (s, CH_3 , 3H), 7.30 (m, C- H_{ar} , 2H), 7.53 (m, C- H_{ar} , 2H). ^{13}C NMR (400 MHz, DMSO- d_6 , δ in ppm): 17.0, 122.9, 127.2, 127.5, 130.6, 131.0, 132.9.

2-(Ethylthio)benzenamine hydrochloride. Yield: 68%. Anal. Calcd for $\text{C}_8\text{H}_{12}\text{NSCl}$ (%): C 50.65; H 6.38; N 7.38. Found (%): C 50.66; H 6.35; N 7.34. M.p. 157–158 °C. FT-IR (KBr pellets, cm^{-1}): 751 [m, $\nu(\text{C-S})$], 2846 [s, $\nu(\text{C-NH}_3^+)$], 1507 [m, $\nu(\text{C-NH}_3^+)$], 1558 [m, $\nu(\text{C=C}_{\text{ar}})$]. ^1H NMR (400 MHz, DMSO- d_6 , δ in ppm): 1.17 (t, CH_3 , 3H), 2.91 (q, CH_2 , 2H), 5.53 (br, C- NH_3^+ , 3H), 7.21 (m, C- H_{ar} , 1H), 7.31 (m, C- H_{ar} , 1H), 7.43 (m, C- H_{ar} , 1H), 7.50 (m, C- H_{ar} , 1H). ^{13}C NMR (400 MHz, DMSO- d_6 , δ in ppm): 14.0, 28.3, 121.9, 125.9, 126.9, 128.1, 133.2, 136.0.

2-(Propylthio)benzenamine hydrochloride. Yield: 83%. Anal. Calcd for $\text{C}_9\text{H}_{14}\text{NSCl}$ (%): C 53.06; H 6.93; N 6.88. Found (%): C 53.00; H 6.92; N 6.82. M.p. 150–153 °C. FT-IR (KBr pellets, cm^{-1}): 748 [s, $\nu(\text{C-S})$], 2846 [s, $\nu(\text{C-NH}_3^+)$], 1473 [m, $\nu(\text{C-NH}_3^+)$], 1572 [m, $\nu(\text{C=C}_{\text{ar}})$]. ^1H NMR (400 MHz, DMSO- d_6 , δ in ppm): 0.93 (t, CH_3 , 3H), 1.54 (sextet, CH_2 , 2H), 2.87 (t, $\text{CH}_2\text{-S}$, 2H), 5.25 (br, C- NH_3^+), 7.18 (m, C- H_{ar} , 1H), 7.26 (m, C- H_{ar} , 1H), 7.41 (m, C- H_{ar} , 1H), 7.49 (m, C- H_{ar} , 1H). ^{13}C NMR (400 MHz, DMSO- d_6 , δ in ppm): 12.9, 22.0, 36.2, 122.0, 126.0, 127.4, 128.0, 133.0, 135.8.

2-(Butylthio)benzenamine hydrochloride. Yield: 94%. Anal. Calcd for $\text{C}_{10}\text{H}_{16}\text{NSCl}$ (%): C 55.16; H 7.41; N 6.43. Found (%): C 55.15; H 7.42; N 6.42. M.p. 141–143 °C. FT-IR (KBr pellets, cm^{-1}): 761 [m, $\nu(\text{C-S})$], 2854 [s, $\nu(\text{C-NH}_3^+)$], 1473 [m, $\nu(\text{C-NH}_3^+)$], 1557 [m, $\nu(\text{C=C}_{\text{ar}})$]. ^1H NMR (400 MHz, DMSO- d_6 , δ in ppm): 0.84 (t, CH_3 , 3H), 1.36 (sextet, CH_2 , 2H), 1.50 (quintet, CH_2 , 2H), 2.91 (t, $\text{CH}_2\text{-S}$, 2H), 5.31 (br, C- NH_3^+ , 3H), 7.23 (m, C- H_{ar} , 1H), 7.28 (m, C- H_{ar} , 1H), 7.43 (m, C- H_{ar} , 1H), 7.51 (m, C- H_{ar} , 1H). ^{13}C NMR (400 MHz, DMSO- d_6 , δ in ppm): 13.4, 21.2, 30.7, 33.8, 122.4, 126.5, 128.0, 132.8, 135.1.

3.4. Synthesis of Iminic Ligands L1C–L4C

Iminic ligands were synthesized in an inert argon atmosphere using dry methanol. Methanolic solutions (10 mL each) of pyridoxal hydrochloride (1.1 mmol, 0.224 g) and the respective *S*-alkylated aniline (1.0 mmol) were mixed in a 50 mL round bottom flask. The resulting mixture was refluxed for 2 h under magnetic stirring. Afterward, the reaction mixture was cooled to room temperature and a methanolic solution (10 mL) of potassium hydroxide (KOH, 2.1 mmol, 0.118 g) was added; the reaction was stirred at room temperature for another 15 min (Scheme 1). The methanol was then evaporated and the product was washed several times with water and then with ethyl ether and hexane. The resulting solid was filtered, recrystallized from methanol, and dried in a desiccator with calcium chloride (CaCl_2). The ligands L2C, L3C, and L4C have been already published in our previous work [23]. The NMR, FT-IR, and UV-Vis spectra of the iminic ligands L1C–L4C are provided in the Supplementary Material.

Ligand L1C: 4-(2-(methylthio)phenylimino)methyl-5-(hydroxymethyl)-2-methylpyridin-3-ol. Yield: 52%. Anal. Calcd. for $\text{C}_{15}\text{H}_{16}\text{N}_2\text{O}_2\text{S}$ (%): C 62.48; H 5.59; N 9.71. Found (%): C 62.46; H 5.60; N 9.73. M.p. 184–185 °C. FT-IR (KBr pellets, cm^{-1}): 755 [m, $\nu(\text{C-S})$], 1606 [m, $\nu(\text{C=N})$], 1581 [w, $\nu(\text{C=C}_{\text{ar}})$], 1201 [s, $\nu(\text{C-O})$]. ^1H NMR (400 MHz, CDCl_3 , δ in ppm): 2.52 (s, CH_3 , 3H), 2.60 (s, CH_3 , 3H), 4.89 (s, 2H, $\text{CH}_2\text{-O}$), 7.21–7.36 (m, C- H_{ar} , 4H), 7.98 (s, C- H_{ar} , 1H), 9.19 (s, $\text{C}_{(\text{imine})}\text{-H}$, 1H). UV-Visible (DMF, λ_{max} in nm; ϵ_{max} in $\text{M}^{-1}\cdot\text{cm}^{-1}$): 272 (15,150). The structure of the L1C ligand can be evaluated in the Supporting Information, Figure S27 and Table S3.

Ligand L2C: 4-(2-(ethylthio)phenylimino)methyl-5-(hydroxymethyl)-2-methylpyridin-3-ol. Yield: 87%. Anal. Calcd. for $\text{C}_{16}\text{H}_{18}\text{N}_2\text{O}_2\text{S}$ (%): C 63.55; H 6.00; N 9.26. Found (%): C 63.52; H 6.02; N 9.25. M.p. 133–134 °C. FT-IR (KBr pellets, cm^{-1}): 750 [m, $\nu(\text{C-S})$], 1606 [m, $\nu(\text{C=N})$], 1581 [m, $\nu(\text{C=C}_{\text{ar}})$], 1282 [s, $\nu(\text{C-O})$]. ^1H NMR (400 MHz, CDCl_3 , δ in ppm): 1.39 (t, CH_3 , 3H), 2.60 (s, CH_3 , 3H), 2.99 (q, S-CH_2 , 2H), 4.88 (s, $\text{CH}_2\text{-O}$, 2H), 7.21–7.41 (m, C- H_{ar} , 4H), 7.95 (s, C- H_{ar} , 1H), 9.16 (s, $\text{C}_{(\text{imine})}\text{-H}$, 1H). UV-Visible (DMF, λ_{max} in nm; ϵ_{max} in $\text{M}^{-1}\cdot\text{cm}^{-1}$): 276 (11,390).

Ligand **L3C**: 4-(2-(propylthio)phenylimino)methyl-5-(hydroxymethyl)-2-methylpyridin-3-ol. Yield: 74%. Anal. Calcd. for $C_{17}H_{20}N_2O_2S$ (%): C 64.53; H 6.37; N 8.85. Found (%): C 64.58; H 6.44; N 8.77. M.p. 131–132 °C. FT-IR (KBr pellets, cm^{-1}): 754 [m, ν (C-S)], 1607 [m, ν (C=N)], 1582 [w, ν (C=C_{ar})], 1286 [m, ν (C-O)]. 1H NMR (400 MHz, $CDCl_3$, δ in ppm): 1.09 (t, CH_3 , 3H), 1.78 (sextet, CH_2 , 2H), 2.61 (s, CH_3 , 3H), 2.96 (t, CH_2 -S, 2H), 4.88 (s, O- CH_2 , 2H), 7.23–7.42 (m, C-H_{ar}, 4H), 7.94 (s, C-H_{ar}, 1H), 9.19 (s, C(imine)-H, 1H). UV-Visible (DMF, λ_{max} in nm; ϵ_{max} in $M^{-1}\cdot cm^{-1}$): 276 (13,370).

Ligand **L4C**: 4-(2-(butylthio)phenylimino)methyl-5-(hydroxymethyl)-2-methylpyridin-3-ol. Yield: 63%. Anal. Calcd. for $C_{18}H_{22}N_2O_2S$ (%): C 65.42; H 6.71; N 8.48. Found (%): C 65.44; H 6.77; N 8.40. M.p. 124–125 °C. FT-IR (KBr pellets, cm^{-1}): 754 [m, ν (C-S)], 1607 [m, ν (C=N)], 1582 [m, ν (C=C_{ar})], 1287 [m, ν (C-O)]. 1H NMR (400 MHz, $CDCl_3$, δ in ppm): 0.97 (t, CH_3 , 3H), 1.52 (sextet, CH_2 , 2H), 1.73 (quintet, CH_2 , 2H), 2.62 (s, CH_3 , 3H), 2.98 (t, CH_2 -S, 2H), 4.88 (s, O- CH_2 , 2H), 7.23–7.41 (m, C-H_{ar}, 4H), 7.96 (s, C-H_{ar}, 1H), 9.18 (s, C(imine)-H, 1H). UV-visible (DMF, λ_{max} in nm; ϵ_{max} in $M^{-1}\cdot cm^{-1}$): 274 (16,770).

3.5. Synthesis of $[Co^{III}(LnC)(LOC)]$ Series Complexes (**C1'**–**C4'**)

3.5.1. Conventional Method

The complexation reactions were carried out in an open atmosphere using methanol without purification. Then, 0.10 mmol of the ligand (**L1C**, 0.029 g; **L2C**, 0.030 g; **L3C**, 0.032 g; **L4C**, 0.033 g) was dissolved in 15 mL of methanol in a 50 mL round bottom flask, and triethylamine (0.10 mmol, 0.010 g, 14 μ L) was added to the solution. Cobalt(II) acetate ($Co^{II}(CH_3COO)_2$, 0.05 mmol, 0.009 g) was then added and the resulting solution was kept under magnetic stirring at 60 °C for 3 h. During this period, air was bubbled into the reaction mixture every hour using an electric pump (Scheme 2). Subsequently, the resulting solution was filtered by simple filtration using filter paper; tetrahydrofuran and acetonitrile (5 mL each) were added to the solution in the **C2'** and **C4'** complexes, respectively.

After slow evaporation of the solvents at room temperature, dark red single crystals suitable for X-ray diffraction were obtained. The crystals were washed with small portions of water and chloroform and then dried in a desiccator with $CaCl_2$. The FT-IR and UV-Vis spectra of the iminic complexes **C1'**–**C4'** are demonstrated in the Supplementary Material. Similar results were obtained in a one-pot version of these reactions (Section 3.5.2).

3.5.2. Alternative One-Pot Synthesis

In a round bottom flask containing methanol (15 mL), pyridoxal (0.10 mmol) and the corresponding amine (0.10 mmol) were added. The resulting mixture was heated to 60 °C and kept under magnetic stirring for 30 min. After this period, upon the addition of triethylamine (0.30 mmol, 0.030 g, 42 μ L) an intense yellow coloration appeared, which changed to dark brown upon addition of cobalt(II) acetate ($Co^{II}(CH_3COO)_2$, 0.05 mmol, 0.009 g). The resulting solution was kept under magnetic stirring at 60 °C for 3 h. During this period, air was bubbled into the reaction mixture every hour (during 5 min) by an electric pump. Subsequently, the resulting solution was filtered by simple filtration through filter paper. Specifically, in the **C2'** and **C4'** complexes, 5 mL of tetrahydrofuran and 5 mL of acetonitrile, respectively, were added to the solution. After slow evaporation of the solvents at room temperature, dark red single crystals suitable for X-ray diffraction were obtained. The crystals were washed with small portions of water and chloroform, and then dried in a desiccator with $CaCl_2$.

Complex $[Co^{III}(L1C)(LOC)]\cdot 4H_2O$ (**C1'**): Crystalline material yield: 25%. MP > 350 °C (decomposition). Elem. Anal. for $C_{29}H_{27}CoN_4O_4S_2\cdot 4H_2O$ (690.66 $g\ mol^{-1}$): Calc. (%): C, 50.43; H, 5.11; N, 8.11. Found (%): C, 50.33; H, 5.03; N, 8.07. FT-IR (KBr, cm^{-1}): 3245 [br, ν (O-H)_{alcohol}], 3002 [w, ν (C-H)_{aromatic}], 2915 [w, ν (C-H)_{aliphatic}], 1602 [s, ν (C=N)_{imine}], 1573 [w, ν (C=C)_{aromatic}], 1266 [m, ν (C-O)_{aromatic}], and 764 [m, ν (C-S)]. UV-Vis, λ_{max} (DMF, ϵ in $M^{-1}\ cm^{-1}$): 272 nm ($\epsilon = 38,900$).

Complex $[Co^{III}(L2C)(LOC)]\cdot THF\cdot CH_3CN$ (**C2'**): Crystalline material yield: 17%. MP \approx 315 °C (decomposition). Elem. Anal. for $C_{30}H_{29}CoN_4O_4S_2\cdot THF\cdot CH_3CN$ (745.78 $g\ mol^{-1}$):

Calc. (%): C, 57.98; H, 5.41; N, 9.39. Found (%): C, 57.35; H, 5.30; N, 9.35. FT-IR (KBr, cm^{-1}): 3185 [br, $\nu(\text{O-H})_{\text{alcohol}}$], 3056 [w, $\nu(\text{C-H})_{\text{aromatic}}$], 1604 [m, $\nu(\text{C=N})_{\text{imine}}$], 1574 [w, $\nu(\text{C=C})_{\text{aromatic}}$], 1265 [m, $\nu(\text{C-O})_{\text{aromatic}}$], and 756 [m, $\nu(\text{C-S})$]. UV-Vis, λ_{max} (DMF, ϵ in $\text{M}^{-1} \text{cm}^{-1}$): 272 nm ($\epsilon = 43,350$).

Complex $[\text{Co}^{\text{III}}(\text{L3C})(\text{L0C})]\cdot\text{MeOH}$ (**C3'**): Crystalline material yield: 15%. MP ≈ 240 °C (decomposition). Elem. Anal. for $\text{C}_{31}\text{H}_{31}\text{CoN}_4\text{O}_4\text{S}_2\cdot\text{MeOH}$ ($678.69 \text{ g mol}^{-1}$): Calc. (%): C, 56.63; H, 5.20; N, 8.25. Found (%): C, 56.69; H, 5.21; N, 8.20. FT-IR (KBr, cm^{-1}): 3202 [br, $\nu(\text{O-H})_{\text{alcohol}}$], 2960 [w, $\nu(\text{C-H})_{\text{aliphatic}}$], 1604 [m, $\nu(\text{C=N})_{\text{imine}}$], 1574 [w, $\nu(\text{C=C})_{\text{aromatic}}$], 1267 [w, $\nu(\text{C-O})_{\text{aromatic}}$], and 754 [m, $\nu(\text{C-S})$]. UV-Vis, λ_{max} (DMF, ϵ in $\text{M}^{-1} \text{cm}^{-1}$): 266 nm ($\epsilon = 47,540$).

Complex $[\text{Co}^{\text{III}}(\text{L4C})(\text{L0C})]$ (**C4'**): Crystalline material yield: 15%. MP > 350 °C. Elem. Anal. for $\text{C}_{32}\text{H}_{33}\text{CoN}_4\text{O}_4\text{S}_2\cdot 4\text{H}_2\text{O}$ ($660.67 \text{ g mol}^{-1}$): Calc. (%): C, 58.17; H, 5.03; N, 8.48. Found (%): C, 58.16; H, 4.95; N, 8.45. FT-IR (KBr, cm^{-1}): 3218 [br, $\nu(\text{O-H})_{\text{alcohol}}$], 2955 [w, $\nu(\text{C-H})_{\text{aliphatic}}$], 1604 [s, $\nu(\text{C=N})_{\text{imine}}$], 1574 [w, $\nu(\text{C=C})_{\text{aromatic}}$], 1267 [m, $\nu(\text{C-O})_{\text{aromatic}}$], and 755 [m, $\nu(\text{C-S})$]. UV-Vis, λ_{max} (DMF, ϵ in $\text{M}^{-1} \text{cm}^{-1}$): 266 nm ($\epsilon = 44,120$).

3.6. Synthesis of $[\text{Co}^{\text{III}}(\text{LnC})_2]\text{PF}_6$ Series Complexes (**C1–C4**)

3.6.1. Conventional Method

The complexation reactions were conducted in an open atmosphere using methanol without purification. Then, 0.10 mmol of the ligand (**L1C**, 0.029 g; **L2C**, 0.030 g; **L3C**, 0.032 g; **L4C**, 0.033 g) was dissolved in 15 mL of methanol in a 50 mL round bottom flask, and triethylamine (0.10 mmol, 0.010 g, 14 μL) was added to the solution. The precursor complex dichlorobis(triphenylphosphane)cobalt(II) ($\text{Co}^{\text{II}}\text{Cl}_2(\text{PPh}_3)_2$, 0.05 mmol, 0.033 g) and potassium(I) hexafluorophosphate (KPF_6 , 0.10 mmol, 0.018 g) were then added. The resulting solution was kept under magnetic stirring at 60 °C for 2 h (Scheme 2). After the reaction, the resulting solution was filtered by simple filtration using filter paper.

In the **C4** complex, ethanol and acetonitrile (2 and 5 mL, respectively) were added to the solution. After slow evaporation of the solvents at room temperature, dark red single crystals suitable for X-ray diffraction were acquired. The crystals were washed with small portions of water and dichloromethane and dried in a desiccator with CaCl_2 . The FT-IR and UV/Vis spectra of the iminic complexes **C1'–C4'** are demonstrated in the Supplementary Material. Similar results were obtained in a one-pot version of these reactions (Section 3.6.2).

3.6.2. Alternative One-Pot Synthesis

In a round bottom flask containing methanol (15 mL), pyridoxal (0.10 mmol) and the corresponding amine (0.10 mmol) were added. The resulting mixture was heated to 60 °C and kept under magnetic stirring for 30 min. After this period, triethylamine (0.30 mmol, 0.030 g, 42 μL) was added, followed by addition of the precursor complex dichlorobis(triphenylphosphane)cobalt(II) ($\text{Co}^{\text{II}}\text{Cl}_2(\text{PPh}_3)_2$, 0.05 mmol, 0.033 g) and potassium(I) hexafluorophosphate (KPF_6 , 0.10 mmol, 0.018 g). The resulting solution was kept under magnetic stirring at 60 °C for 2 h. After the reaction, the resulting solution was filtered by simple filtration through filter paper. Specifically, in the **C4** complex, 2 mL of ethanol and 5 mL of acetonitrile were added to the solution. After slow evaporation of the solvents at room temperature, dark red single crystals suitable for X-ray diffraction were obtained. The crystals were washed with small portions of water and dichloromethane, and then dried in a desiccator with calcium(II) chloride.

Complex $[\text{Co}^{\text{III}}(\text{L1C})_2]\text{PF}_6\cdot\text{H}_2\text{O}\cdot\text{MeOH}\cdot 2(\text{C}_7\text{H}_9\text{NS})$ (**C1**): Crystalline material yield: 71%. MP > 350 °C. Elem. Anal. for $\text{C}_{30}\text{H}_{30}\text{CoF}_6\text{N}_4\text{O}_4\text{PS}_2\cdot\text{H}_2\text{O}\cdot\text{MeOH}\cdot 2(\text{C}_7\text{H}_9\text{NS})$ ($1107.08 \text{ g mol}^{-1}$): Calc. (%): C, 48.87; H, 4.92; N, 7.59. Found (%): C, 48.88; H, 4.95; N, 7.45. FT-IR (KBr, cm^{-1}): 2980 [w, $\nu(\text{C-H})_{\text{aliphatic}}$], 1604 [m, $\nu(\text{C=N})_{\text{imine}}$], 1574 [w, $\nu(\text{C=C})_{\text{aromatic}}$], 1273 [m, $\nu(\text{C-O})_{\text{aromatic}}$], 842 [s, $\nu(\text{PF}_6^-)$], and 770 [w, $\nu(\text{C-S})$]. UV-Vis, λ_{max} (DMF, ϵ in $\text{M}^{-1} \text{cm}^{-1}$): 274 nm ($\epsilon = 37,910$).

Complex $[\text{Co}^{\text{III}}(\text{L2C})_2]\text{PF}_6$ (**C2**): Crystalline material yield: 78%. MP ≈ 287 °C (decomposition). Elem. Anal. for $\text{C}_{32}\text{H}_{34}\text{CoF}_6\text{N}_4\text{O}_4\text{PS}_2$ ($806.65 \text{ g mol}^{-1}$): Calc. (%): C, 47.65;

H, 4.25; N, 6.95 Found (%): C, 47.61; H, 4.22; N, 6.95. FT-IR (KBr, cm^{-1}): 2929 [w, $\nu(\text{C}-\text{H})_{\text{aliphatic}}$], 1605 [s, $\nu(\text{C}=\text{N})_{\text{imine}}$], 1573 [w, $\nu(\text{C}=\text{C})_{\text{aromatic}}$], 1266 [m, $\nu(\text{C}-\text{O})_{\text{aromatic}}$], 845 [s, $\nu(\text{PF}_6^-)$], and 771 [m, $\nu(\text{C}-\text{S})$]. UV-Vis, λ_{max} (DMF, ϵ in $\text{M}^{-1} \text{cm}^{-1}$): 266 nm ($\epsilon = 37,830$).

Complex $[\text{Co}^{\text{III}}(\text{L3C})_2]\text{PF}_6$ (**C3**): Crystalline material yield: 86%. MP > 350 °C. Elem. Anal. for $\text{C}_{34}\text{H}_{38}\text{CoF}_6\text{N}_4\text{O}_4\text{PS}_2$ ($834.70 \text{ g mol}^{-1}$): Calc. (%): C, 48.92; H, 4.59; N, 6.71 Found (%): C, 48.89.; H, 4.05; N, 6.66. FT-IR (KBr, cm^{-1}): 2965 [w, $\nu(\text{C}-\text{H})_{\text{aliphatic}}$], 1605 [s, $\nu(\text{C}=\text{N})_{\text{imine}}$], 1574 [w, $\nu(\text{C}=\text{C})_{\text{aromatic}}$], 1266 [m, $\nu(\text{C}-\text{O})_{\text{aromatic}}$], 840 [s, $\nu(\text{PF}_6^-)$], and 771 [w, $\nu(\text{C}-\text{S})$]. UV-Vis, λ_{max} (DMF, ϵ in $\text{M}^{-1} \text{cm}^{-1}$): 274 nm ($\epsilon = 35,560$).

Complex $[\text{Co}^{\text{III}}(\text{L4C})_2]\text{PF}_6 \cdot \text{EtOH} \cdot \text{CH}_3\text{CN}$ (**C4**): Crystalline material yield: 90%. MP ≈ 250 °C (decomposition). Elem. Anal. for $\text{C}_{38}\text{H}_{43}\text{CoF}_6\text{N}_4\text{O}_4\text{PS}_2 \cdot \text{CH}_3\text{CN} \cdot \text{EtOH}$ ($948.87 \text{ g mol}^{-1}$): Calc. (%): C, 50.58; H, 5.41; N, 7.37 Found (%): C, 50.59; H, 5.40; N, 7.39. FT-IR (KBr, cm^{-1}): 2960 [w, $\nu(\text{C}-\text{H})_{\text{aliphatic}}$], 1604 [s, $\nu(\text{C}=\text{N})_{\text{imine}}$], 1574 [m, $\nu(\text{C}=\text{C})_{\text{aromatic}}$], 1267 [m, $\nu(\text{C}-\text{O})_{\text{aromatic}}$], 841 [s, $\nu(\text{PF}_6^-)$], and 770 [w, $\nu(\text{C}-\text{S})$]. UV-Vis, λ_{max} (DMF, ϵ in $\text{M}^{-1} \text{cm}^{-1}$): 276 nm ($\epsilon = 43,850$).

3.7. In Silico Calculations

The crystallographic structure of DNA and HSA were obtained from Protein Data Bank (PDB) with access codes 1BNA and 1N5U, respectively [73,74]. The three-dimensional structural spike glycoprotein of SARS-CoV-2 (wild type) with the three RBD in down conformation, one in up conformation, and in complex with the cellular ACE2 were also obtained from the PDB with the access codes 6VXX, 6VYB, and 7KJ2, respectively. The chemical structure of **C1'-C4'** and **C1-C4** were obtained from the experimental X-ray data, while the superoxide ions (O_2^-) were built and energy minimized with the Density Functional Theory (DFT) method with Becke-3-Lee Yang Parr (B3LYP) and standard 6-31G* basis set, available in the Spartan'18 software (Wavefunction, Inc., Irvine, CA, USA).

The molecular docking calculations were performed with GOLD 2020.2 software (Cambridge Crystallographic Data Center Software Ltd., Cambridge, UK). Hydrogen atoms were added to the biomacromolecules following tautomeric states and ionization data inferred by the software. The DNA structure has two possible binding sites (major and minor groove), which were explored in the docking calculation (8.0 Å spherical cavity around each region) [56,75]. On the other hand, the HSA structure presents three main binding pockets, which were also explored by in silico calculations (8.0 Å spherical cavity around subdomains IIA, IIIA, and IB) [76], while for the superoxide dismutase mimetic activity (complexes **C1'-C4'** and **C1-C4**), a 5.0 Å spherical cavity around Co^{III} was defined, and for RBD of SARS-CoV-2 a 10 Å spherical cavity was delimited around the three domains. The number of genetic operations (crossing, migration, and mutation) during the search procedure was set as 100,000. For the scoring function, ChemPLP was used, which is a default function of the GOLD 2020.2 software. The figures of the docking poses for the largest docking score values were generated with the PyMOL Delano Scientific LLC software (DeLano Scientific LLC: San Carlos, CA, USA).

4. Conclusions

Derivatizations of the thiol functions of 2-aminothiophenol through alkylation reactions using different haloalkanes (iodomethane, bromoethane, 1-bromopropane, and 1-bromobutane) in an alkaline medium were done to obtain S-alkylated anilines with the thioether function bonded to aliphatic chains with one to four carbons. Afterward, these compounds had their amine functions condensed with pyridoxal hydrochloride to obtain four iminic organic ligands (**L1C-L4C**). The ligands **L1C-L4C** showed tridentate chelating behavior due to the presence of phenolate oxygen (after deprotonation), imine nitrogen, and thioether sulfur atoms that acted as donor atoms. Thus, when reacting such ligands with cobalt cations in a 2:1 ratio (ligand/cobalt), octahedral complexes were formed by the coordination of two units of the tridentate ligands to the Co^{III} metallic center.

By using Co^{II} acetate, the formation of a series $[\text{Co}^{\text{III}}(\text{LnC})(\text{LOC})]$ ($n = 1-4$, **C1'-C4'**) was observed, with the coordination of a ligand unit presenting scission of the C-S bond and,

consequently, a thiolate function (L0C) resulting in neutral Co^{III} complexes. Nevertheless, when the reaction was carried out using the $\text{CoCl}_2(\text{PPh}_3)_2$ complex and adding KPF_6 , no scission of the C-S bonds occurred, forming a series $[\text{Co}^{\text{III}}(\text{LnC})_2]\text{PF}_6$ ($n = 1-4$, **C1-C4**) composed of ionic Co^{III} complexes in the form of a KPF_6 salt. Overall, this exciting method allows the synthesis of Co^{III} complexes without cleavage of the C-S bonds from the ligands, thereby not requiring an inert atmosphere in the reaction systems. Given our findings, it is highly suggested to extend this study to iminic ligands derived from 2-aminothiophenol derivatized with branched aliphatic chains, including *tert*-butyl, to observe the possible occurrence of C-S cleavage in these derivatives and evaluate the effectiveness of using $\text{CoCl}_2(\text{PPh}_3)_2$ to avoid this possible cleavage behavior in these cases.

The best docking score values for DNA were obtained into the minor groove, suggesting that Co^{III} complexes can interact with DNA not via intercalative behavior. Unexpectedly, the increase in carbon in the S-alkyl portions of the Co^{III} complexes improved their DNA interaction profile (**C4** and **C4'**). However, based on the literature, the Co^{III} complexes under study showed docking score values comparable with the experimental capacity of other cobalt complexes to interact with DNA. Additionally, there was a good correlation between the binding capacity of the inorganic complexes with DNA and their SOD-mimetic capability (interaction with $\text{O}_2^{\cdot-}$). Finally, all Co^{III} complexes might be biodistributed in the human bloodstream by has, and mainly **C4** and **C4'** showed a feasible trend of interaction with the spike glycoprotein of SARS-CoV-2 with RBD in a down conformation, suggesting the possibility of Co^{III} complexes to act as anticancer/antiviral metallodrugs.

Supplementary Materials: The following supporting information can be downloaded at: <https://www.mdpi.com/article/10.3390/inorganics12060171/s1>, Table S1. Crystal data and data collection and refinements of complexes **C1'-C4'**; Table S2. Crystal data and data collection and refinements of complexes **C1-C4**; Figure S1. ^1H NMR spectra of the 2-(Methylthio)aniline hydrochloride (DMSO-d_6 , 400 MHz, 25 °C). Figure S2. ^{13}C NMR spectra of the 2-(Methylthio)aniline hydrochloride (DMSO-d_6 , 100 MHz, 25 °C). Figure S3. ^1H NMR spectra of the 2-(Ethylthio)benzenamine hydrochloride (DMSO-d_6 , 400 MHz, 25 °C). Figure S4. ^{13}C NMR spectra of the 2-(Ethylthio)benzenamine hydrochloride (DMSO-d_6 , 100 MHz, 25 °C). Figure S5. ^1H NMR spectra of the 2-(Propylthio)benzenamine hydrochloride (DMSO-d_6 , 400 MHz, 25 °C). Figure S6. ^{13}C NMR spectra of the 2-(Propylthio)benzenamine hydrochloride (DMSO-d_6 , 100 MHz, 25 °C). Figure S7. ^1H NMR spectra of the 2-(Butylthio)benzenamine hydrochloride (DMSO-d_6 , 400 MHz, 25 °C). Figure S8. ^{13}C NMR spectra of the 2-(Butylthio)benzenamine hydrochloride (DMSO-d_6 , 100 MHz, 25 °C). Figure S9. ^1H NMR spectra of the ligand **L1C** (CDCl_3 , 400 MHz, 25 °C). Impurities: 5.30 (dichloromethane); 3.46 (methanol) and 1.61 (residual water). Figure S10. ^1H NMR spectra of the ligand **L2C** (CDCl_3 , 400 MHz, 25 °C). Impurities: 5.30 (dichloromethane) and 1.64 (residual water). Figure S11. ^1H NMR spectra of the ligand **L3C** (CDCl_3 , 400 MHz, 25 °C). Figure S12. ^1H NMR spectra of the ligand **L4C** (CDCl_3 , 400 MHz, 25 °C). Figure S13. Steady state UV-Vis spectra of ligand **L1C**, complex **C1'** and complex **C1** (Experimental conditions: DMF, room temperature, 10^{-5} M range). Figure S14. Steady state UV-Vis spectra of ligand **L2C**, complex **C2'** and complex **C2** (Experimental conditions: DMF, room temperature, 10^{-5} M range). Figure S15. Steady state UV-Vis spectra of ligand **L3C**, complex **C3'** and complex **C3** (Experimental conditions: DMF, room temperature, 10^{-5} M range). Figure S16. Steady state UV-Vis spectra of ligand **L4C**, complex **C4'** and complex **C4** (Experimental conditions: DMF, room temperature, 10^{-5} M range). Figure S17. Infrared spectra (FTIR) of the S-alkylated aniline 2-(methylthio)aniline hydrochloride. Figure S18. Infrared spectra (FTIR) of the ligand **L1C**. Figure S19. Infrared spectra (FTIR) of the complex **C1'**. Figure S20. Infrared spectra (FTIR) of the complex **C2'**. Figure S21. Infrared spectra (FTIR) of the complex **C3'**. Figure S22. Infrared spectra (FTIR) of the complex **C4'**. Figure S23. Infrared spectra (FTIR) of the complex **C1**. Figure S24. Infrared spectra (FTIR) of the complex **C2**. Figure S25. Infrared spectra (FTIR) of the complex **C3**. Figure S26. Infrared spectra (FTIR) of the complex **C4**. Figure S27. ORTEP-3.1 projection of the molecular structures of the ligand **L1C** in the solid state. Ellipsoids were calculated at 50% probability. Table S3. Crystal data and data collection and refinements of ligand **L1C**. Supplementary data: CCDC 2245356–2245359, 2245360–2245362, 2245364, and 2245365 contain the supplementary crystallographic data for complexes **C1'-C4'**, **C1-C3**, **C4** and, **LC1** respectively. These data can be obtained free of charge via <http://www.ccdc.cam.ac.uk/conts/retrieving.html>, accessed

on 6 June 2024, or from the Cambridge Crystallographic Data Centre, 12 Union Road, Cambridge CB2 1EZ, UK; fax: (+44) 1223-336-033; or e-mail: deposit@ccdc.cam.ac.uk.

Author Contributions: Conceptualization, O.A.C. and D.F.B.; methodology, L.A.F., F.M.M., J.D.S., O.A.C. and D.F.B.; software, O.A.C. and C.S.; validation, O.A.C. and D.F.B.; formal analysis, L.A.F., F.M.M., J.D.S., O.A.C. and D.F.B.; investigation, L.A.F., F.M.M., J.D.S., O.A.C. and D.F.B.; resources, D.F.B.; data curation, O.A.C. and D.F.B.; writing—original draft preparation, D.F.B.; writing—review and editing, C.S., O.A.C. and D.F.B.; visualization, D.F.B.; supervision, D.F.B.; project administration, D.F.B.; funding acquisition, D.F.B. All authors have read and agreed to the published version of the manuscript.

Funding: This research was funded by the Brazilian Research Councils, Conselho Nacional do Desenvolvimento Científico e Tecnológico (CNPq, Edital PQ 06/2019 and 309482/2019-4) and Coordenação de Aperfeiçoamento de Pessoal de Nível Superior (CAPES-PROEX, 001). This research was also funded by the Portuguese Agency for Scientific Research, Fundação para a Ciência e a Tecnologia (FCT), through the projects UIDB/00313/2020 (<https://doi.org/10.54499/UIDB/00313/2020>, accessed on 15 February 2024) and UIDP/00313/2020 (<https://doi.org/10.54499/UIDP/00313/2020>, accessed on 15 February 2024).

Data Availability Statement: Data are contained within the article.

Acknowledgments: The authors acknowledge Atlas Assessoria Linguística (Santa Maria, RS, Brazil) for the language editing. O.A.C. also thanks FCT for his PhD fellowship 2020.07504.BD (<https://doi.org/10.54499/2020.07504.BD>, accessed on 15 February 2024).

Conflicts of Interest: The authors declare no conflicts of interest.

References

1. Biswas, S.; Kumar Manna, C.; Naskar, R.; Das, A.; Mondal, T.K. Synthesis of new rhodium(III) complex by benzylic CS bond cleavage of thioether containing NNS donor Schiff base ligand: Investigation of catalytic activity towards transfer hydrogenation of ketones. *Inorg. Chim. Acta* **2021**, *515*, 120096. [[CrossRef](#)]
2. Wang, L.; He, W.; Yu, Z. Transition-metal mediated carbon–sulfur bond activation and transformations. *Chem. Soc. Rev.* **2013**, *42*, 599–621. [[CrossRef](#)] [[PubMed](#)]
3. Lou, J.; Wang, Q.; Wu, P.; Wang, H.; Zhou, Y.-G.; Yu, Z. Transition-metal mediated carbon–sulfur bond activation and transformations: An update. *Chem. Soc. Rev.* **2020**, *49*, 4307–4359. [[CrossRef](#)] [[PubMed](#)]
4. Bag, J.; Barman, S.; Maiti, B.K.; Pal, K. M(II) (M=Cu, Ni) Assisted C–S bond cleavage and oxidative dehydrogenation of amine on non-innocent salen type ligand platforms by varying nitrogen vs. sulfur coordination atoms. *Eur. J. Inorg. Chem.* **2022**, *11*, e202101107. [[CrossRef](#)]
5. Wongnate, T.; Ragsdale, S.W. The reaction mechanism of methyl-coenzyme M reductase. *J. Biol. Chem.* **2015**, *290*, 9322–9334. [[CrossRef](#)] [[PubMed](#)]
6. Pattanayak, P.; Patra, D.; Brandão, P.; Mal, D.; Felix, V. Synthesis and characterization of palladium(II) complex of Schiff base ligand: CS bond cleavage and catalytic activity. *Inorg. Chem. Commun.* **2015**, *53*, 68–71. [[CrossRef](#)]
7. Biswas, S.; Roy, P.; Mondal, T.K. Synthesis of palladium(II) complex with NNS donor Schiff base ligand via C S bond cleavage: X-ray structure, electrochemistry and DFT computation. *J. Mol. Struct.* **2017**, *1142*, 110–115. [[CrossRef](#)]
8. Elsby, M.R.; Ghostine, K.; Das, U.K.; Gabidullin, B.M.; Baker, R.T. Iron-SNS and -CNS complexes: Selective caryl–S bond cleavage and amine-borane dehydrogenation catalysis. *Organometallics* **2019**, *38*, 3844–3851. [[CrossRef](#)]
9. Roy, P.; Manna, C.K.; Naskar, R.; Mondal, T.K. Synthesis of a rhodium(III) triphenylphosphine complex via C S bond cleavage of an azo-thioether ligand: X-ray structure, electrochemistry and catalysis towards transfer hydrogenation of ketones. *Polyhedron* **2019**, *158*, 208–214. [[CrossRef](#)]
10. Majouga, A.G.; Beloglazkina, E.K.; Moiseeva, A.A.; Shilova, O.V.; Manzhelii, E.A.; Lebedeva, M.A.; Davies, E.S.; Khlobystov, A.N.; Zyk, N.V. Cleavage of the C–S bond with the formation of a binuclear copper complex with 2-thiolato-3-phenyl-5-(pyridine-2-ylmethylene)-3,5-dihydro-4H-imidazole-4-one. A new mimic of the active site of N₂O reductase. *Dalton Trans.* **2013**, *42*, 6290. [[CrossRef](#)]
11. Chakraborty, P.; Chandra, S.K.; Chakravorty, A. Ring-size specific transformations of cobalt(III)-thioether chelates activated by base. Co-C formation or C-S cleavage? *Organometallics* **1993**, *12*, 4726–4727. [[CrossRef](#)]
12. Chakraborty, P.; Karmakar, S.; Chandra, S.K.; Chakravorty, A. New cobalt complexes incorporating thioether chelation and base-induced homolog-selective transformations thereof. *Inorg. Chem.* **1994**, *33*, 816–822. [[CrossRef](#)]
13. Rajsekhar, G.; Rao, C.P.; Saarenketo, P.K.; Kolehmainen, E.; Rissanen, K. C–S bond cleavage by cobalt: Synthesis, characterization and crystal structure determination of 1,2-di-(o-salicylaldiminophenylthio)ethane and its Co(III) product with C–S bond cleaved fragments. *Inorg. Chem. Commun.* **2002**, *5*, 649–652. [[CrossRef](#)]

14. Rajsekhar, G.; Rao, C.P.; Saarenketo, P.; Nättinen, K.; Rissanen, K. Complexation behaviour of hexadentate ligands possessing N_2O_4 and $N_2O_2S_2$ cores: Differential reactivity towards Co(II), Ni(II) and Zn(II) salts and structures of the products. *New J. Chem.* **2004**, *28*, 75–84. [[CrossRef](#)]
15. Singh, A.K.; Mukherjee, R. Cobalt(II) and cobalt(III) complexes of thioether-containing hexadentate pyrazine amide ligands: C–S bond cleavage and cyclometallation reaction. *Dalton Trans.* **2008**, *14*, 260–270. [[CrossRef](#)] [[PubMed](#)]
16. Cleave, C.V.; Crans, D.C. The first-row transition metals in the periodic table of medicine. *Inorganics* **2019**, *7*, 111. [[CrossRef](#)]
17. Osman, D.; Cooke, A.; Young, T.R.; Deery, E.; Robinson, N.J.; Warren, M.J. The requirement for cobalt in vitamin B12: A paradigm for protein metalation. *Biochim. Biophys. Acta Mol. Cell Res.* **2021**, *1868*, 118896. [[CrossRef](#)] [[PubMed](#)]
18. Ge, Y.; Zadeh, M.; Mohamadzadeh, M. Vitamin B12 regulates the transcriptional, metabolic, and epigenetic programming in human ileal epithelial cells. *Nutrients* **2022**, *14*, 2825. [[CrossRef](#)] [[PubMed](#)]
19. Froese, D.S.; Fowler, B.; Baumgartner, M.R. Vitamin B12, folate, and the methionine remethylation cycle—Biochemistry, pathways, and regulation. *J. Inherit. Metab. Dis.* **2019**, *42*, 673–685. [[CrossRef](#)]
20. Renfrew, A.K.; O'Neill, E.S.; Hambley, T.W.; New, E.J. Harnessing the properties of cobalt coordination complexes for biological application. *Coord. Chem. Rev.* **2018**, *375*, 221–233. [[CrossRef](#)]
21. Acharyya, K.; Mukherjee, P.S. Organic imine cages: Molecular marriage and applications. *Angew. Chem. Int. Ed.* **2019**, *58*, 8640–8653. [[CrossRef](#)]
22. Basak, D.; van Leusen, J.; Gupta, T.; Kögerler, P.; Bertolasi, V.; Ray, D. Unusually distorted pseudo-octahedral coordination environment around Co^{II} from thioether Schiff base ligands in dinuclear $[CoLn]$ ($Ln = La, Gd, Tb, Dy, Ho$) complexes: Synthesis, structure, and understanding of magnetic behavior. *Inorg. Chem.* **2020**, *59*, 2387–2405. [[CrossRef](#)]
23. Fontana, L.A.; Stüker, M.; Oliveira, G.M.; Iglesias, B.A.; Back, D.F. Pro-oxidant activity of nickel (II) pyridoxal complexes. Synthesis, characterization and peroxidase activity assays. *Inorg. Chem. Commun.* **2015**, *62*, 55–59. [[CrossRef](#)]
24. Rocha, J.F.; Pina, A.F.; Sousa, S.F.; Cerqueira, N.M.F.S.A. PLP-dependent enzymes as important biocatalysts for the pharmaceutical, chemical and food industries: A structural and mechanistic perspective. *Catal. Sci. Technol.* **2019**, *9*, 4864–4876. [[CrossRef](#)]
25. Casas, J.S.; Couce, M.D.; Sordo, J. Coordination chemistry of vitamin B6 and derivatives: A structural overview. *Coord. Chem. Rev.* **2012**, *256*, 3036–3062. [[CrossRef](#)]
26. Naskar, S.; Naskar, S.; Butcher, R.J.; Chattopadhyay, S.K. Synthesis, X-ray crystal structures and spectroscopic properties of two Ni(II) complexes of pyridoxal Schiff's bases with diamines: Importance of steric factor in stabilization of water helices in the lattices of metal complex. *Inorg. Chim. Acta* **2010**, *363*, 404–411. [[CrossRef](#)]
27. Siqueira, J.D.; de Pellegrin, S.F.; dos Santos, S.S.; Iglesias, B.A.; Piquini, P.C.; Arantes, L.P.; Soares, F.A.; Chaves, O.A.; Neves, A.; Back, D.F. SOD activity of new copper II complexes with ligands derived from pyridoxal and toxicity in *Caenorhabditis elegans*. *J. Inorg. Biochem.* **2020**, *204*, 110950. [[CrossRef](#)]
28. Anthony, E.J.; Bolitho, E.M.; Bridgewater, H.E.; Carter, O.W.L.; Donnelly, J.M.; Imberti, C.; Lant, E.C.; Lermyte, F.; Needham, R.J.; Palau, M.; et al. Metallodrugs are unique: Opportunities and challenges of discovery and development. *Chem. Sci.* **2020**, *11*, 12888–12917. [[CrossRef](#)]
29. Kabir, E.; Noyan, M.R.O.K.; Hossain, M.A. Synthesis, biological and medicinal impacts of metallodrugs: A study. *Res. Chem.* **2023**, *5*, 100935. [[CrossRef](#)]
30. Szeffler, B.; Czelen, P. Will the Interactions of Some Platinum (II)-Based Drugs with B-Vitamins Reduce Their Therapeutic Effect in Cancer Patients? Comparison of Chemotherapeutic Agents such as Cisplatin, Carboplatin and Oxaliplatin—A Review. *Int. J. Mol. Sci.* **2023**, *24*, 1548. [[CrossRef](#)]
31. Zhang, C.; Xu, C.; Gao, X.; Yao, Q. Platinum-based drugs for cancer therapy and anti-tumor strategies. *Theranostics* **2022**, *12*, 2115–2132. [[CrossRef](#)]
32. Komlyagina, V.I.; Romashev, N.F.; Besprozvannykh, V.K.; Arakelyan, J.; Wu, C.; Chubarov, A.S.; Bakaev, I.V.; Soh, Y.K.; Abramov, P.A.; Cheung, K.L.; et al. Effects of bis(imino)acenaphthene (bian)-derived ligands on the cytotoxicity, DNA interactions, and redox activity of palladium(II) bipyridine complexes. *Inorg. Chem.* **2023**, *62*, 11541–11553. [[CrossRef](#)]
33. Bian, M.; Fan, R.; Yang, Z.; Chen, Y.; Xu, Z.; Lu, Y.; Liu, W. Pt(II)-NHC complex induces ROS-ERS-related DAMP balance to harness immunogenic cell death in hepatocellular carcinoma. *J. Med. Chem.* **2022**, *65*, 1848–1866. [[CrossRef](#)]
34. Phan, T.T.V.; Huynh, T.-C.; Manivasagan, P.; Mondal, S.; Oh, J. An up-to-date review on biomedical applications of palladium nanoparticles. *Nanomaterials* **2020**, *10*, 66. [[CrossRef](#)]
35. Mirzaei, S.; Hushmandi, K.; Zabolian, A.; Saleki, H.; Torabi, S.M.R.; Ranjbar, A.; SeyedSaleh, S.; Sharifzadeh, S.O.; Khan, H.; Ashrafzadeh, M.; et al. Elucidating role of reactive oxygen species (ROS) in cisplatin chemotherapy: A focus on molecular pathways and possible therapeutic strategies. *Molecules* **2021**, *26*, 2382. [[CrossRef](#)]
36. Perillo, B.; Di Donato, M.; Pezone, A.; Di Zazzo, E.; Giovannelli, P.; Galasso, G.; Castoria, G.; Migliaccio, A. ROS in cancer therapy: The bright side of the moon. *Exp. Mol. Med.* **2020**, *52*, 192–203. [[CrossRef](#)]
37. Carneiro, T.J.; Martins, A.S.; Marques, M.P.M.; Gil, A.M. Metabolic aspects of palladium(II) potential anti-cancer drugs. *Front. Oncol.* **2020**, *12*, 590970. [[CrossRef](#)]
38. Jahankhani, K.; Ahangari, F.; Adcock, I.M.; Mortaz, E. Possible cancer-causing capacity of COVID-19: Is SARS-CoV-2 an oncogenic agent? *Biochimie* **2023**, *213*, 130–138. [[CrossRef](#)]
39. Li, J.; Bai, H.; Qiao, H.; Du, C.; Yao, P.; Zhang, Y.; Cai, Y.; Jia, Y.; Wei, X.; Li, C.; et al. Causal effects of COVID-19 on cancer risk: A Mendelian randomization study. *J. Med. Virol.* **2023**, *95*, e28722. [[CrossRef](#)]

40. Ghosh, M.K.; Kumar, S.; Ganguly, K.K.; Ghosh, P.; Tabassum, S.; Basu, B.; Basu, M. COVID-19 and cancer: Insights into their association and influence on genetic and epigenetic landscape. *Epigenomics* **2023**, *15*, 227–248. [[CrossRef](#)]
41. Casini, A.; Pothig, A. Metals in cancer research: Beyond platinum metallodrugs. *ACS Cent. Sci.* **2024**, *10*, 242–250. [[CrossRef](#)] [[PubMed](#)]
42. Yousuf, I.; Bashir, M.; Arjmand, F.; Tabassum, S. Advancement of metal compounds as therapeutic and diagnostic metallodrugs: Current frontiers and future perspectives. *Coord. Chem. Rev.* **2021**, *445*, 214104. [[CrossRef](#)]
43. Kar, K.; Ghosh, D.; Kabi, B.; Chandra, A. A concise review on cobalt Schiff base complexes as anticancer agents. *Polyhedron* **2022**, *222*, 115890. [[CrossRef](#)]
44. Smilowicz, D.; Metzler-Nolte, N. Bioconjugates of Co(III) complexes with Schiff base ligands and cell penetrating peptides: Solid phase synthesis, characterization and antiproliferative activity. *J. Inorg. Biochem.* **2020**, *206*, 111041. [[CrossRef](#)] [[PubMed](#)]
45. Kaushik, S.; Paliwal, S.K.; Iyer, M.R.; Patil, V.M. Promising Schiff bases in antiviral drug design and discovery. *Med. Chem. Res.* **2023**, *32*, 1063–1076. [[CrossRef](#)] [[PubMed](#)]
46. Chang, E.L.; Simmers, C.; Knight, D.A. Cobalt complexes as antiviral and antibacterial agents. *Pharmaceuticals* **2010**, *3*, 1711–1728. [[CrossRef](#)] [[PubMed](#)]
47. Costanzo, M.; de Giglio, M.A.R.; Roviello, G.N. Deciphering the relationship between SARS-CoV-2 and cancer. *Int. J. Mol. Sci.* **2023**, *24*, 7803. [[CrossRef](#)] [[PubMed](#)]
48. Tyler, L.A.; Olmstead, M.M.; Mascharak, P.K. Conversion of azomethine moiety to carboxamido group at cobalt(III) center in model complexes of Co-containing nitrile hydratase. *Inorg. Chem.* **2001**, *40*, 5408–5414. [[CrossRef](#)] [[PubMed](#)]
49. Yang, F.; Zhou, Q.; Zhang, Y.; Zeng, G.; Li, G.; Shi, Z.; Wang, B.; Feng, S. Inspiration from old molecules: Field-induced slow magnetic relaxation in three air-stable tetrahedral cobalt(II) compounds. *Chem. Commun.* **2013**, *49*, 5289. [[CrossRef](#)]
50. Pattanayak, P.; Pratihar, J.L.; Patra, D.; Lin, C.-H.; Paul, S.; Chakraborty, K. Synthesis, characterization, structure, redox property, antibacterial and catalytic activity of tridentate Schiff base cobalt(III), nickel(II) and palladium(II) complexes. *Polyhedron* **2013**, *51*, 275–282. [[CrossRef](#)]
51. Chaves, O.A.; Rodrigues-Santos, C.E.; Echevarria, Á.; Sacramento, C.Q.; Fintelman-Rodrigues, N.; Temerozo, J.R.; Castro-Faria-Neto, H.C.; E Souza, T.M.L. Fluorine atoms on C₆H₅-corrole affect the interaction with Mpro and PLpro proteases of SARS-CoV-2: Molecular docking and 2D-QSAR approaches. *Int. J. Mol. Sci.* **2022**, *23*, 10936. [[CrossRef](#)]
52. Enyedy, I.J.; Egan, W.J. Can we use docking and scoring for hit-to-lead optimization? *J. Comput. Aided Mol. Des.* **2008**, *22*, 161–168. [[CrossRef](#)]
53. Basourakos, S.P.; Li, L.; Aparicio, A.M.; Corn, P.G.; Kim, J.; Thompson, T.C. Combination platinum-based and DNA damage response-targeting cancer therapy: Evolution and future directions. *Curr. Med. Chem.* **2017**, *24*, 1586–1606. [[CrossRef](#)]
54. Brulikova, J.; Hlavac, J.; Hradil, P. DNA interstrand cross-linking agents and their chemotherapeutic potential. *Curr. Med. Chem.* **2012**, *19*, 364–385. [[CrossRef](#)]
55. Martin, L.P.; Hamilton, T.C.; Schilder, R.J. Platinum resistance: The role of DNA repair pathways. *Clin. Cancer Res.* **2008**, *14*, 1291–1295. [[CrossRef](#)]
56. Martins, F.M.; Siqueira, J.D.; Iglesias, B.A.; Chaves, O.A.; Back, D.F. Pyridoxal water-soluble cobalt(II) helicates: Synthesis, structural analysis, and interactions with biomacromolecules. *J. Inorg. Biochem.* **2022**, *233*, 111854. [[CrossRef](#)]
57. Griess, B.; Tom, E.; Domann, F.; Teoh-Fitzgerald, M. Extracellular superoxide dismutase and its role in cancer. *Free Rad. Biol. Med.* **2017**, *112*, 464–479. [[CrossRef](#)]
58. Sheng, Y.; Abreu, I.A.; Cabell, D.E.; Maroney, M.J.; Miller, A.-F.; Teixeira, M.; Valentine, J.S. Superoxide dismutases and superoxide reductases. *Chem. Rev.* **2014**, *114*, 3854–3918. [[CrossRef](#)]
59. Siqueira, J.D.; de Pellegrin, S.F.; Fontana, L.A.; Iglesias, B.A.; Sagrillo, M.R.; Oliveira, P.S.; Rossato, A.; da Silva Silveira, L.; Neves, A.; Chaves, O.A.; et al. Copper (II) complexes derived from pyridoxal: Structural correlations, cytotoxic activities, and molecular docking. *Inorg. Chim. Acta* **2021**, *526*, 120530. [[CrossRef](#)]
60. Chaves, O.A.; Iglesias, B.A.; Serpa, C. Biophysical characterization of the interaction between a transport human plasma protein and the 5,10,15,20-tetra(pyridine-4-yl)porphyrin. *Molecules* **2022**, *27*, 5341. [[CrossRef](#)]
61. Naveenraj, S.; Anandan, S. Binding of serum albumins with bioactive substances–Nanoparticles to drugs. *J. Photochem. Photobiol. C* **2013**, *14*, 53–71. [[CrossRef](#)]
62. Chaves, O.A.; Acunha, T.V.; Iglesias, B.A.; Jesus, C.S.H.; Serpa, C. Effect of peripheral platinum(II) bipyridyl complexes on the interaction of tetra-cationic porphyrins with human serum albumin. *J. Mol. Liq.* **2020**, *301*, 112466. [[CrossRef](#)]
63. Da Silveira, C.H.; Chaves, O.A.; Marques, A.C.; Rosa, N.M.P.; Costa, L.A.S.; Iglesias, B.A. Synthesis, photophysics, computational approaches, and biomolecule interactive studies of metalloporphyrins containing pyrenyl units: Influence of the metal center. *Eur. J. Inorg. Chem.* **2022**, *12*, e202200075. [[CrossRef](#)]
64. Sarmiento, C.O.; Pinheiro, B.F.A.; Abrahão, J.; Chaves, O.A.; Moreira, M.B.; Nikolaou, S. Interactions of a ruthenium-ketoprofen compound with human serum albumin and DNA: Insights from spectrophotometric titrations and molecular docking calculations. *ChemistrySelect* **2022**, *7*, e202104020. [[CrossRef](#)]
65. Tisoco, I.; Donatoni, M.C.; Victória, H.F.V.; de Toledo, J.R.; Krambrock, K.; Chaves, O.A.; de Oliveira, K.T.; Iglesias, B.A. Photophysical, photooxidation, and biomolecule-interaction of meso-tetra(thienyl)porphyrins containing peripheral Pt(II) and Pd(II) complexes. Insights for photodynamic therapy applications. *Dalton Trans.* **2022**, *51*, 1646–1657. [[CrossRef](#)] [[PubMed](#)]

66. Parvarinezhad, S.; Salehi, M.; Kubicki, M.; Malekshah, R.E. Experimental and theoretical studies of new Co(III) complexes of hydrazide derivatives proposed as multi-target inhibitors of SARS-CoV-2. *Appl. Organomet. Chem.* **2022**, *36*, e6836. [[CrossRef](#)] [[PubMed](#)]
67. Ioannou, K.; Vlasidou, M.C. Metal-based complexes against SARS-CoV-2. *Biometals* **2022**, *35*, 639–652. [[CrossRef](#)] [[PubMed](#)]
68. El-Lateef, H.M.A.; El-Dabea, T.; Khalaf, M.M.; Abu-Dief, A.M. Development of metal complexes for treatment of coronaviruses. *Int. J. Mol. Sci.* **2022**, *23*, 6418. [[CrossRef](#)] [[PubMed](#)]
69. Yan, R.; Zhang, Y.; Li, Y.; Ye, F.; Guo, Y.; Xia, L.; Zhong, X.; Chi, X.; Zhou, Q. Structural basis for the different states of the spike protein of SARS-CoV-2 in complex with ACE2. *Cell Res.* **2021**, *31*, 717–719. [[CrossRef](#)]
70. Sheldrick, G.M. A short history of SHELX. *Acta Cryst.* **2008**, *64*, 112–122. [[CrossRef](#)]
71. Sheldrick, G.M. Crystal structure refinement with SHELXL. *Acta Cryst.* **2015**, *71*, 3–8.
72. Farrugia, L.J. ORTEP-3 for Windows—A version of ORTEP-III with a Graphical User Interface (GUI). *J. Appl. Cryst.* **1997**, *30*, 565. [[CrossRef](#)]
73. Drew, H.R.; Wing, R.M.; Takano, T.; Broka, C.; Tanaka, S.; Itakura, K.; Dickerson, R.E. Structure of a B-DNA dodecamer: Conformation and dynamics. *Proc. Natl. Acad. Sci. USA* **1981**, *78*, 2179–2183. [[CrossRef](#)] [[PubMed](#)]
74. Wardell, M.; Wang, Z.; Ho, J.X.; Robert, J.; Ruker, F.; Ruble, J.; Carter, D.C. The atomic structure of human methemalbumin at 1.9 Å. *Biochem. Biophys. Res. Commun.* **2002**, *291*, 813–819. [[CrossRef](#)] [[PubMed](#)]
75. Siqueira, J.D.; de Pellegrin, S.F.; Fioravanco, L.P.; Fontana, L.A.; Iglesias, B.A.; Chaves, O.A.; Back, D.F. Self-association synthesis with ortho-vanillin to promote mono- and heptanuclear complexes and their evaluation as antioxidant agents. *J. Mol. Struct.* **2022**, *1256*, 132480. [[CrossRef](#)]
76. Soares, M.A.G.; de Aquino, P.A.; Costa, T.; Serpa, C.; Chaves, O.A. Insights into the effect of glucose on the binding between human serum albumin and the nonsteroidal anti-inflammatory drug nimesulide. *Int. J. Biol. Macromol.* **2024**, *265*, 131148. [[CrossRef](#)]

Disclaimer/Publisher’s Note: The statements, opinions and data contained in all publications are solely those of the individual author(s) and contributor(s) and not of MDPI and/or the editor(s). MDPI and/or the editor(s) disclaim responsibility for any injury to people or property resulting from any ideas, methods, instructions or products referred to in the content.